SN 2017gci: a nearby Type I Superluminous Supernova with a bumpy tail

A. Fiore [1,2]★ T.-W. Chen,[3,4] A. Jerkstrand,[3] S. Benetti [1]★ R. Ciolfi [1,5]★ C. Inserra [6] E. Cappellaro,[1]
A. Pastorello,[1] G. Leloudas,[7] S. Schulze [8] M. Berton [9,10] J. Burke,[11,12] C. McCully,[12] W. Fong,[13]
L. Galbany [14] M. Gromadzki,[15] C. P. Gutiérrez [16] D. Hiramatsu,[11,12] G. Hosseinzadeh,[17]
D. A. Howell,[11,12] E. Kankare,[18] R. Lunnan,[3] T. E. Müller-Bravo [16] D. O' Neill,[19] M. Nicholl,[20,21]
A. Rau,[4] J. Sollerman,[3] G. Terreran,[13] S. Valenti[22] and D. R. Young[19]

Affiliations are listed at the end of the paper

ABSTRACT

We present and discuss the optical spectrophotometric observations of the nearby ($z = 0.087$) Type I superluminous supernova (SLSN I) SN 2017gci, whose peak K-corrected absolute magnitude reaches $M_g = -21.5$ mag. Its photometric and spectroscopic evolution includes features of both slow- and of fast-evolving SLSN I, thus favoring a continuum distribution between the two SLSN-I subclasses. In particular, similarly to other SLSNe I, the multiband light curves (LCs) of SN 2017gci show two re-brightenings at about 103 and 142 d after the maximum light. Interestingly, this broadly agrees with a broad emission feature emerging around 6520 Å after ∼51 d from the maximum light, which is followed by a sharp knee in the LC. If we interpret this feature as Hα, this could support the fact that the bumps are the signature of late interactions of the ejecta with a (hydrogen-rich) circumstellar material. Then we fitted magnetar- and CSM-interaction-powered synthetic LCs on to the bolometric one of SN 2017gci. In the magnetar case, the fit suggests a polar magnetic field $B_p \simeq 6 \times 10^{14}$ G, an initial period of the magnetar $P_{\text{initial}} \simeq 2.8$ ms, an ejecta mass $M_{\text{ejecta}} \simeq 9\,M_\odot$ and an ejecta opacity $\kappa \simeq 0.08\,\text{cm}^2\,\text{g}^{-1}$. A CSM-interaction scenario would imply a CSM mass $\simeq 5\,M_\odot$ and an ejecta mass $\simeq 12\,M_\odot$. Finally, the nebular spectrum of phase $+187$ d was modeled, deriving a mass of $\sim 10\,M_\odot$ for the ejecta. Our models suggest that either a magnetar or CSM interaction might be the power sources for SN 2017gci and that its progenitor was a massive ($40\,M_\odot$) star.

Key words: Transients: supernovae – supernova: general – supernovae: individual: SN 2017gci.

1 INTRODUCTION

Superluminous supernovae (SLSNe) were initially defined as those supernovae (SNe) whose peak-absolute magnitude is brighter than –21 mag (Gal-Yam 2012). They are intrinsically rare objects often discovered in metal-poor dwarf host galaxies (Chen et al. 2013; Lunnan et al. 2014; Leloudas et al. 2015; Perley et al. 2016; Chen et al. 2017a; Schulze et al. 2018). The origin of such peculiar transients represents a major challenge for contemporary astrophysics since it raises some fundamental questions about the ultimate stages of the evolution of massive stars. From an observational point of view, SLSNe can be broadly classified according to their hydrogen abundance. SLSNe I are H poor, although some of them display a late ($\gtrsim 100$ d) occurrence of Hα (a fraction estimated to be ~ 15 per cent, Yan et al. 2017), while Type II SLSNe display Balmer lines in their optical spectra. Recently, it has been proposed that $M_g = -19.8$ mag can be used as a luminosity threshold for the SLSNe I subclass only (Gal-Yam 2019). However, this does not seem to correspond to a sharp edge in the luminosity function of H-poor SNe (De Cia et al. 2018; Quimby et al. 2018; Gal-Yam 2019) and the SLSN I

classification is generally inferred with a spectrum taken at about the maximum luminosity. This is characterized by a hot blue continuum (with a blackbody temperature $T_{\text{BB}} \simeq 10\,000$–$15\,000$ K) with O II absorptions between 3000 and 5000 Å.

Determining which physical mechanisms drive the explosion of a SLSN is not obvious. Therefore, the discovery of nearby SLSNe (with $z \lesssim 0.1$) is of particular interest since it may allow for higher resolution spectra, possibly in a wider wavelength range. A handful of viable scenarios have been invoked to explain the luminosity of SLSNe, as e.g. the onset of the pair-instability mechanism (e.g. Yoshida et al. 2016) in very massive stars (heavier than $\sim 130\,M_\odot$, Rakavy & Shaviv 1967; Gal-Yam et al. 2009). In such a scenario, the central pressure drop caused by the e^+, e^- pair creation promptly triggers the collapse of the star and the thermonuclear explosion of its core with an overwhelming production of nickel. None the less, the amount of ^{56}Ni mass required for an absolute peak-magnitude brighter than ~ -21 mag could make the rise time of the light curves (LCs) too slow (Nicholl et al. 2013) compared to the observations. Moreover, the spectra of the slow SLSNe I cannot be fitted by pair-instability models (Dessart et al. 2013; Jerkstrand, Smartt & Heger 2016). Another possibility lies in the interaction of the SN ejecta with a circumstellar material (CSM, e.g. Chevalier & Fransson 2003; Chevalier & Irwin 2011; Chatzopoulos, Wheeler & Vinko 2012; Ginzubrg & Balberg 2012; Chatzopoulos et al. 2013; Nicholl et al.

★ E-mail: achille.fiore@inaf.it (AF); stefano.benetti@inaf.it (SB); riccardo.ciolfi@inaf.it (RC)

2014; Chen et al. 2015) which was lost by the progenitor star, e.g. via stellar winds or during a pulsational pair-instability phase. If so, the SN ejecta crashes into surrounding shells or clumps of dense matter and drives a shock at the collision edge. This can convert the kinetic energy of the SN ejecta to radiation. However, there are generally no 'standard' spectroscopic signatures (i.e. narrow emission lines, as in the case of Type IIn (SL)SNe, e.g. SN 2006gy, Smith et al. 2007) of CSM interaction in the spectra of SLSNe I (Lunnan et al. 2019). On the other hand, the presence of the intermediate-width Mg II resonance doublet around ∼2800 Å (Lunnan et al. 2018), the late broad Hα emission (Yan et al. 2015) and the LC oscillations (bumps) of some SLSNe I (Nicholl et al. 2015; Yan et al. 2017) strongly support that the interaction with CSM must be taken into account.

Finally, a model that has growing consensus within the astrophysical community considers that the luminosity of SLSNe I is sustained by the spin-down radiation of a nascent magnetar (e. g. Kasen & Bildsten 2010; Woosley 2010; Suzuki & Maeda 2017, 2019). According to this scenario, a highly magnetized, newly born neutron star is the compact remnant left by the SLSN explosion. Similarly to the case of a pulsar-wind nebula (e.g. Metzger et al. 2014), the energy radiated by the neutron star via magnetic-dipole braking inflates a low-density, radiation-dominated photon-pair plasma nebula that afterwards thermalizes into the expanding ejecta, thus acting as a (possibly dominant) power source to explain the luminosity of SLSNe I. The magnetar scenario is favoured also by the association of the superluminous SN 2011kl (Greiner et al. 2015) with an ultralong gamma-ray burst. Initially, it was proposed that SLSNe I might share the environment with fast radio bursts (FRBs) (Nicholl et al. 2017; Margalit et al. 2018) but the recent discovery of two FRBs with a massive host galaxy (Ravi et al. 2019; Marcote et al. 2020) disfavours this association.

SLSNe I are actually a heterogeneous class of transients. In fact, it is possible to distinguish between at least two subclasses, depending on whether their LCs evolve in a slow or a fast fashion. Slow-evolving SLSNe I have a rise time towards the maximum luminosity which exceeds 50 d, whereas the fast-evolving SLSNe I reach the maximum light in less than 30 d. Although a continuum distribution likely fills the gap between the two subclasses (Nicholl et al. 2015; De Cia et al. 2018), the distinction between fast- and slow-evolving SLSNe I is still used (e.g. Kumar et al. 2020) and helpful to distinguish different rise or decline time-scales within the SLSN I class. In addition, slow-evolving SLSNe I more often show bumps in their LC both before and after the maximum-luminosity epoch (Inserra et al. 2017; Inserra 2019).

SN 2017gci is located at RA = $06^h46^m45^s.02$ and Dec. = $-27°14'55''.8$ (J2000). It was discovered by *Gaia* on the 2017 August 16, (Delgado et al. 2017) as an apparently hostless, blue transient, and named Gaia17cbp. Initially, it was classified as a cataclysmic variable-candidate. Later, it was reclassified as SLSN I (Lyman et al. 2017) by the extended Public ESO Spectroscopic Survey for Transient Objects (ePESSTO, Smartt et al. 2015). The last g'-, r'-, i'-, z'-, J-, H-, K_s-band imaging frames (taken on 2019 September 29) show that the host-galaxy flux contribution of SN 2017gci is not completely negligible at optical/near-infrared (NIR) wavelengths ($g_{host} \simeq 22.8$ mag, $r_{host} \simeq 22.2$ mag, $i_{host} \simeq 22$ mag, $J_{host} \simeq 21.6$ mag, $H_{host} \simeq 21.5$ mag, see Section 2).

We hereby present the LCs and the spectra of the SLSN I SN 2017gci. The observations will be made public via WiseRep.[1]

In addition, we provide an interpretation of the data both with a semi-analytic magnetar-powered modelling and by means of the single-zone SUMO models (Jerkstrand et al. 2017) for the nebular spectra of SLSNe I. Hereafter, in Section 2, we describe and discuss the photometric observations; Section 3 deals with the spectra of SN 2017gci; in Section 4, we compare the spectra and the LCs of SN 2017gci with those ones of other SLSNe I and we provide our interpretation of this event within the CSM and the magnetar scenarii; finally, we summarize our conclusion in Section 5. Throughout the paper, we assume a flat Universe with $\Omega_m = 0.31$ and $H_0 = 71 \pm 3$ km s^{-1} Mpc^{-1}. Given such cosmological parameters and a redshift $z = 0.0873 \pm 0.0003$ (see Section 3.2), we found a luminosity distance for SN 2017gci of $d_L = 392.5^{+23.5}_{-15.9}$ Mpc, corresponding to a distance modulus $\mu = 37.96 \pm 0.1$ mag. Moreover, we assume no extinction from the host galaxy since no narrow absorption interstellar line of the Na ID doublet (Poznanski et al. 2012) is seen in the optical spectra.

2 PHOTOMETRY

2.1 Observations and preliminary reduction

We performed most of the photometric follow-up with the MPG 2.2-m telescope + GROND (Gamma-Ray Burst Optical and Near-Infrared Detector, Greiner et al. 2008) as a part of GREAT survey (Chen et al. 2018) and with NTT + EFOSC2 (Buzzoni et al. 1984). Premaximum- and maximum-epoch data are scarce, but some epochs near the peak were obtained thanks to the photometry of the Las Cumbres Observatory[2] (LCO) Global Telescope network. These observations were obtained with the camera Sinistro (Brown et al. 2011) built for the 1-m class LCO telescopes. The set of photometric data, we have collected consists of g'-, r'-, i'-, z'-, J-, H-, K_s-band images taken at ESO La Silla Observatory with 2.2-m + GROND, B-, V-, g-, r-, i-, z-filter images taken at LCO, $UVW2$-, $UVM2$-, $UVW1$-, U-, B-, V-filter images obtained with the *Swift* Ultraviolet/Optical Telescope (UVOT) and J-, H-, K_s-filter frames obtained with NTT + SOFI (Son OF Isaac, Moorwood et al. 1998). To preredue the EFOSC2 frames, we applied standard overscan, bias and flat-fielding procedures within IRAF. The SOFI frames were prereduced with the PESSTO pipeline (Smartt et al. 2015). The GROND images were prereduced by the GROND pipeline (Krühler et al. 2008), which applies de-bias and flat-field corrections, stacks images, and provides astrometry calibration.

2.2 Data reduction

We corrected the i and z EFOSC2 frames for the fringing pattern by means of fringing masks. These were created by downloading and reducing ∼100 archival i and z images from the European Southern Observatory (ESO) Archive Science Facility[3] for each filter at random coordinates, and selecting those with an exposure time $\gtrsim 100$ s. We took the median of all of them in order to get rid of the field stars present in the frames. After subtracting the median value from each averaged image, we obtained the master fringing mask to be subtracted to the frames.

B-, g-, V-, r-, i-, z-, J-, H-, K_s-filter magnitudes were measured using the SNOOPY package (Cappellaro 2014) with the point spread function (PSF)-fitting technique, via the DAOPHOT tool (Stetson

---

[1]https://wiserep.weizmann.ac.il/search/.

[2]https://lco.global/.
[3]http://archive.eso.org/.

1987). Within this method, a reference PSF is obtained by averaging those ones of isolated field stars and then fitted on to the SN to obtain the instrumental magnitude. Meanwhile, the background underneath the SN can be estimated interpolating a low-order polynomial to the surrounding regions. In alternative, we removed the host galaxy contribution with the template-subtraction technique, which was also performed within SNOOPY, and via the HOTPANTS package (Becker 2015). The template-subtraction method envisages the subtraction of the scientific frames with a template image of the same field taken with the same filter when the SN is absent. After the template subtraction, the magnitudes are always derived with the PSF method in the residual frame. We found that the template subtraction method gives indeed more reliable photometric measurements, especially when the SN flux becomes fainter. For SN 2017gci, this happens at ϕ $\sim$100 d after maximum. In Tables A1–A4 if not differently stated, the reported magnitudes have been derived after template subtraction.

The g-, r-, i-, z-template frames were downloaded from the Image Cutout Server[4] of the second Data Release of Pan-STARRS as stack images. Deep B, V-template frames were requested to LCO which observed the field of SN 2017gci on 2019 October, 4th (corresponding to 708 rest-frame d after maximum). For the J, H, K_s template frames, we used the combination of the last GROND J-, H-, K_s-band frames taken on 2019 September 25 (700 rest-frame days after the maximum) and 29th (703 rest-frame days after the maximum), assuming that at these very late epochs SN 2017gci faded well below the detection limit. Since the host galaxy is not visible in the deep frame taken about 2 yr after explosion, we estimated an upper limit for the K_s magnitude ($K_{host, uplim} \simeq 18.6$ mag) of the host galaxy using the PSF technique. Hence, we decided to use B, g, V, r, i, z, J, H template-subtracted magnitudes and K PSF magnitudes.

B, g, V, r, i, z magnitudes were calibrated on the field stars identified with the Pan-STARRS (Panoramic Survey Telescope and Rapid Response System, Chambers et al. 2016) catalogue. The calibration was performed after having applied the colour correction (see equation 6 in Tonry et al. 2012) between Pan-STARRS and SDSS filters. For the B, V images the calibration was done after having converted the Pan-STARRS magnitudes to Sloan as before, and then the Sloan magnitudes to Johnsons system following Chonis & Gaskell (2008). The NIR magnitudes were instead calibrated with a local sequence of stars from the Two-Micron All Sky Survey (Skrutskie et al. 2006).

To measure $UVW2$, $UVM2$, $UVW1$, U, B, V *Swift*/UVOT magnitudes, we stacked the layers of the individual observing segments with the task UVOTIMSUM and measured the brightness using 5-arcsec radius aperture with the task UVOTSOURCE in HEASOFT version 6.25 (NASA High Energy Astrophysics Science Archive Research Center (Heasarc) 2014).

Since we have used several instruments to collect the photometry of SN 2017gci, each one defining its own photometric system, it is necessary to convert all of them into a standard one. The procedure involved is sometimes called S-correction (Stritzinger et al. 2002) and we applied it following the method described in Elias-Rosa et al. (2006) and Pignata et al. (2004). Therefore, we computed synthetic photometry using the observed-frame spectra by means of the library PYSYNPHOT[5] both for the standard photometric systems ($m_{s,standard}$) and for the instrumental filters ($m_{s,instr}$).[6] For each instrument and
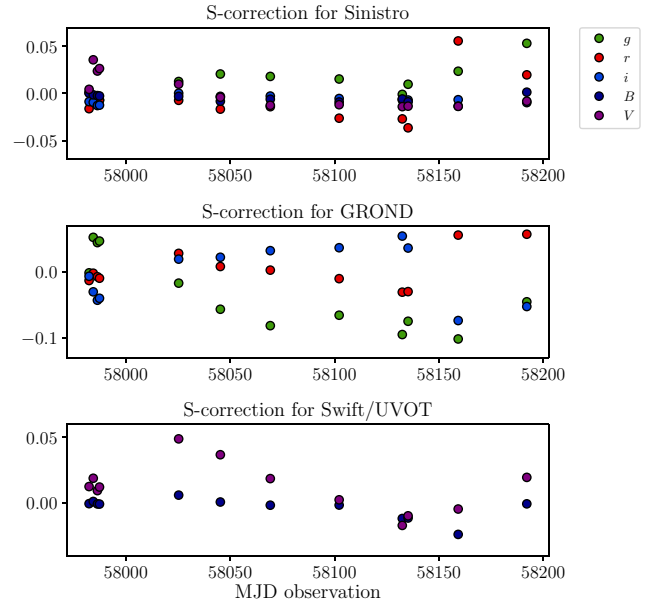
Figure 1 S-correction for LCO+Sinistro (top panel), GROND + 2.2 m (middle panel) and *Swift*/UVOT (lower panel). Filled dots are coded as in the label (top right-hand corner).

each bandpass filter, the S-correction S_{corr} was then computed as $S_{corr} = m_{s,standard} - m_{s,instr}$. We linearly interpolated over the spectroscopic epochs the S_{corr} grid to match the photometric epochs and then we applied the corresponding correction. We estimated a mean statistical uncertainty for this correction by looking at the dispersion around the interpolation and we assumed it to be 0.02 mag. This uncertainty was eventually summed in quadrature with the photometric one to have the final error (see Fig. 1). However, the above procedure can be performed only when the passband filters are entirely covered by the wavelength range of the spectra. If this is not the case (U, z, J, H, K_s), we computed the S-correction as before but using blackbody spectral energy distribution (SED) reported to the observer frame. We considered two ranges of temperature: $T =$ 12000–8000 K up to 40d and $T =$ 8000–4000 K at later phases, broadly corresponding to the blackbody temperatures derived from the SED blackbody fit (see Section 4.3.3). The maximum of the S-correction computed in the adopted range is taken as a proxy of the S-correction error introduced by the non-standard system, which we called ΔS_{corr}. The ΔS_{corr} values were propagated in our analysis. The reduced $UVW2$, $UVM2$, $UVW1$, U, B, g, V, r, i, z, J, H, K_s magnitudes are reported in Table A1–A4. The S-corrections S_{corr} and the ΔS_{corr} values are listed in Table A5–A8. The latter were divided for simplicity in two bins ($4000 < T < 8000$ K and $8000 < T < 12000$ K).

The S-corrected LCs of SN 2017gci are shown in Fig. 2. Magnitudes are in AB system and the phases are corrected for time dilation (in the following, we will refer to the rest-frame phase with respect to maximum luminosity as ϕ). From our photometric data, it is not possible to provide a robust estimate for the maximum luminosity and the corresponding epoch due to a lack of early-time coverage. To obtain an upper limit on the rise time, we added a non-detection from the *Gaia*-archival data (Gaia collaboration 2016a, b; Salgado et al. 2017), whose epoch is 2017 June 27 (MJD = 57931), which was

Figure 2. S-corrected LCs of SN 2017gci in *UVW*2, *UVM*2, *UVW*1, *U*, *B*, *g*, *V*, *r*, *i*, *z*, *J*, *H*, K_s bands plotted in black, brown, cyan, dark green, dark blue, green, purple, red, blue, magenta, orange, silver, and yellow, respectively. Magnitudes obtained with different instruments were plotted with different symbols, as labelled in grey in the upper right-hand corner. The green dotted line represents a fourth-order polynomial fit of the early LC to estimate the maximum epoch in *g* band. Dotted lines represent the linear fit to the data with rest-frame phases later then 74 d, while solid lines represent the linear fits once the bumps have been excluded as explained in the text. The latter points are plotted as empty dots. Arrows correspond to 2.5σ detection limits. Magnitudes are in AB system.

converted to *g* magnitude.[7] Then a fourth-order polynomial was fit over the early *g*-filter magnitudes allowing us to estimate the epoch and magnitude of maximum luminosity: $MJD_{max} = 57990.3^{+8}_{-15}$ for $g_{max} = 17.1 \pm 0.3$ mag.

2.2.1 K-correction

For the optical magnitudes, we obtained the *K*-corrections from the spectra at our disposal (see Section 3). For each of them and for each band-pass filter, we derived a synthetic magnitude via PYSYNPHOT. This was done both for the rest-frame spectrum (for which we computed a synthetic magnitude $m_{s,rest}$) and for the observed one (for which we computed a synthetic magnitude $m_{s,obs}$) via PYSYNPHOT distributed via AstroConda.[8] For each epoch, the *K*-correction *K* was computed as $K = m_{s,obs} - m_{s,rest}$. The resulting *K*-corrections are listed in Table A9. Finally, to adjust the sparser time sampling of the spectral epochs to the denser one of the magnitudes we linearly interpolated this table. Similarly, the *K*-corrections for the *UVW*2-, *UVM*2-, *UVW*1-, *J*, *H*, K_s-filter magnitudes were estimated by using the SED (retrieved by photometry) in place of the observed spectra.

2.3 Main characteristics of the LCs and of the bolometric curve

The *g*-, *V*-, *r*-, *i*-filters LCs remain nearly constant for the first ~20 d, while the *B* LC starts to decline earlier (after about ~12 d from the maximum light). The *U* − and *UVW*2-, *UVM*2-, *UVW*1-filters LCs possibly peak a few days before, but the early-time data coverage is inadequate and so we cannot securely constrain the maximum-luminosity epoch for those filters. The overall evolution is slower

in the *z*, *J*, *H*, K_s magnitudes, and the early flat phase around the maximum luminosity lasts about 30–40 d. Then for $\phi \gtrsim 17$ d, the evolution steepens and at $\simeq 54$–57 d the observed LCs present an abrupt change of their slopes. Such a 'knee' seems much sharper than the transition region which usually preludes to the so-called 'magnetar tail' (see e.g. Inserra et al. 2013; De Cia et al. 2018). Thereafter, for $\phi \gtrsim 71$ d, the LCs settle on a steady, almost linear decline. During this phase, the LCs display two sharp re-brightenings at $\phi \sim 103$ and 142 d. Finally, after $\phi > 213$ d, the SN is no longer detectable. After this epoch, we took four frames in the *g*, *r*, *i*, *z* bands, 3 in *J*-, 2 in *H*- and 1 in K_s GROND bands until 2019 September 29 (see Introduction). However, the template subtracted images provided only 2.5σ detection limits.

Apparent magnitudes were converted to absolute magnitudes once the redshift and the Galactic absorption are known. Given a Galactic extinction $A_G^V = 0.360$ mag (Schlafly & Finkbeiner 2011), the distance modulus μ and the *g* apparent magnitude for the maximum given in Section 1, the *K*-corrected absolute peak-magnitude is $M_g = -21.5 \pm 0.3$ mag in *g* band. We also built the pseudo-bolometric LC of SN 2017gci (see Fig. 3). This was computed by integrating its *K*-corrected *UVW*2, *UWM*2, *UVW*1, *U*, *B*, *g*, *V*, *r*, *i*, *z*, *J*, *H*, K_s photometry. We adopted as reference the epochs of the *r*-band photometry, and missing measurements at given epochs for the other filters were obtained through interpolation or, if necessary, by extrapolation assuming a constant colour from the closest available epoch. The fluxes at the filter effective wavelengths, corrected for the Galactic extinction, provide the SED at each epoch. Then, we integrate the SED with the trapezoidal rule, assuming zero flux at the integration boundaries.

We measured the early and late luminosity-decay slopes on to the bolometric LC. The steeper early decline (between $\phi = 30$–51 d from the maximum light) is estimated to be 0.040 mag d^{-1}, whereas the late one (between $\phi = 60$–210 d from the maximum light) is 0.018 mag d^{-1}. As mentioned above, a handful of SLSNe I (e.g. SN 2015bn, Nicholl et al. 2016a) show a bumpy LC. To measure the post-maximum decay slope for $\phi \gtrsim 73$ d, we excluded the bumps from the linear fit. To do that, we proceeded in the following way.

---

[7]Useful relationships to convert *Gaia* magnitudes to those of the standard photometric systems are available in section 5.3.5 of the Documentation Release (v. 1.2) of the Gaia Data Release 1. This is accessible from the following URL: https://gea.esac.esa.int/archive/documentation/GDR1/.

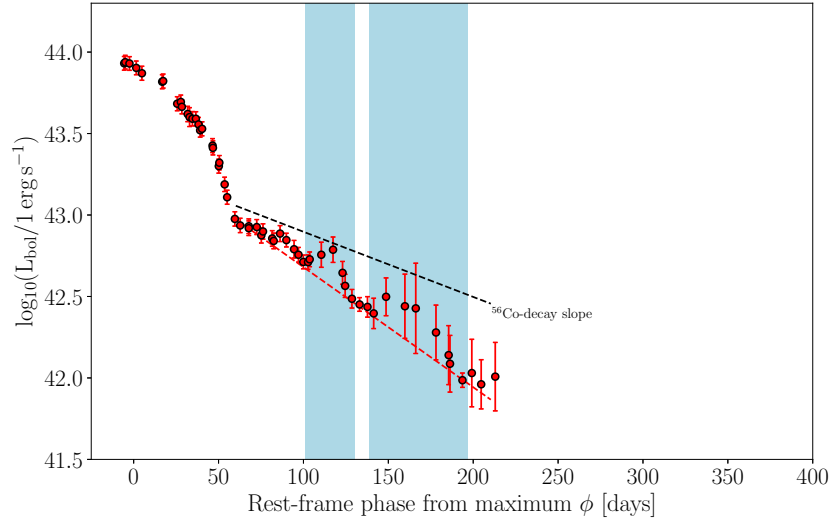[8]https://astroconda.readthedocs.io/en/latest/.

Figure 3. Pseudo-bolometric LC of SN 2017gci (computed after having applied the S-corrections and the *K*-corrections to multiband photometry, see the text). Red dots: pseudo-bolometric LC obtained integrating the SED with the trapezoidal rule. Luminosities are in logarithmic scale and arrows correspond to 2.5σ limits. The light-blue shaded areas refer to the epochs during which the bumps occur.
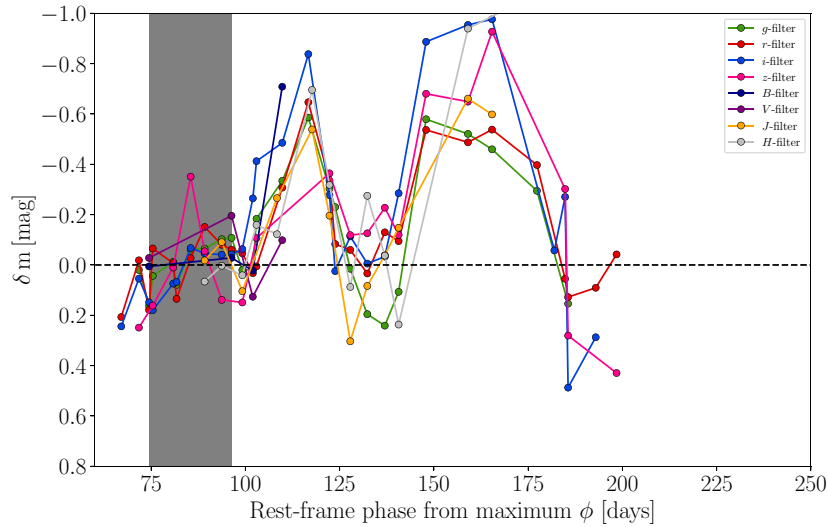

Figure 4. Luminosity undulations δm in each bandpass filter. Datapoints are coloured as in Fig. 2. The dashed black line marks the $\delta m = 0$ mag level. The grey-shaded area represents the phase range within which we consider the LC decline not to be affected by the bump features. Therein, we computed the standard deviation of the linear-fitting residuals to disentangle the bumps (see the text) from the LC decline.

For a given wavelength band, we fitted a first-order polynomial using all the magnitudes for $\phi > 73$ d, and for each of those epochs we subtracted the interpolated magnitude to the corresponding observed one. Then, we computed the standard deviation σ_{73-103} of the fit residuals for $73 \lesssim \phi \lesssim 103$ d (corresponding to the grey shaded area in Fig. 4), since at these epochs the magnitudes do not seem to be affected much by the bumps. At this point we repeated the linear fit, this time excluding all the magnitudes whose difference with the previous fit is brighter than $1 \times \sigma_{73-103}$ mag. Bluer LCs tend to decay faster than the redder ones (except for the *i* and *z* bands). None the less, we specify that the slope estimates for the *B*, *V*, *J*, *H*, K_s LCs are less accurate because of the evident data paucity. The late-decline slopes were not measured for the *UVW*2, *UVM*2, *UWV*1, *U*-filter LCs since no coeval measure is available. The luminosity excesses in the different bands δm over the late post-

peak decline rate $\langle m \rangle$ are such that $|\delta m| = |\langle m \rangle - m| \lesssim 1$ mag (see Fig. 4).

3 SPECTROSCOPY

3.1 Observations and data reduction

Optical spectra were acquired with the ESO New Technology Telescope (NTT)+EFOSC2 at La Silla Observatory, Chile, the ESO Very Large Telescope (VLT) + X-Shooter(XS) (see Vernet et al 2011, for a description) at Paranal Observatory, Chile, the Keck I telescope + LRIS (Oke et al 1995) at W. M. Keck Observatory, Maunakea, Hawaii and the Multiple Mirror Telescope (MMT) + Binospec (Fabricant et al. 2019) at Maunakea Observatory. The EFOSC2, Binospec, and LRIS spectra were reduced with the
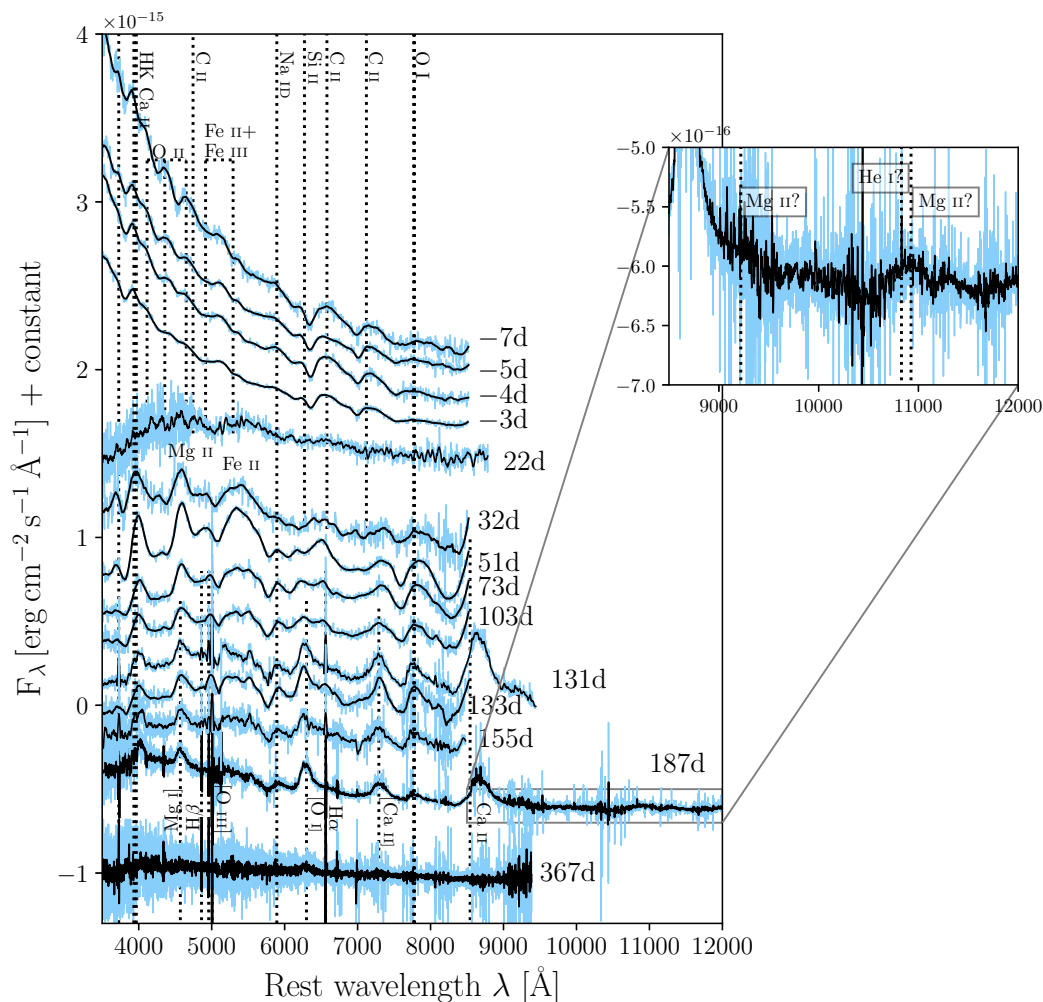
Figure 5. Spectral evolution of SN 2017gci. On the right-hand side, we plotted the rest-frame phase from the discovery for each spectrum. To provide a clear representation, we smoothed the spectra with a Savitzky–Golay filter. The smoothed spectra (black lines) have been overimposed to the original ones (light-blue lines), and all of them were scaled and offset. The black dashed lines mark the wavelengths at which the spectral features occur in the spectra. For each of them, the ion responsible of the transition is labelled nearby. In the last two spectra (at $\phi = 187\,367$ d), the narrow emission lines [O III], Hα, Hβ were cut up to a certain flux threshold. The epochs of the observations, the scaling factors and the offsets are summarized in Table A11. The insert in the upper right-hand corner zooms the NIR part of the XS spectrum taken at 187 d.

standard IRAF tools. Also, five LCO + FLOYDS spectra were secured (see Table A11).

The two-dimensional raw spectroscopic frames were then corrected for overscan, divided by a normalized flat-field, corrected for cosmic rays (by means of the L. A. COSMIC algorithm, Van Dokkum 2001), extracted across the spatial direction after having interpolated the background below the SN with a low-order polynomial fit on the surrounding regions, calibrated in wavelength against HeAr arcs. Then the extracted one-dimensional spectra were calibrated in flux and corrected for telluric absorption thanks to a set of spectrophotometric standard stars. Finally, the flux calibration of these spectra was also checked against the magnitudes retrieved by coeval photometry. The first XS spectrum ($\phi = 187$ d) was reduced following the procedure described in Krühler et al. (2015), whereas the second one ($\phi = 367$ d) was reduced via the ESOREFLEX ESO pipeline (v 2.9.1, Freudling et al. 2013).

3.2 The spectra

The spectral evolution of SN 2017gci is shown in Fig. 5. In order to increase the signal-to-noise ratio, we included in Fig. 5 the average between the spectra observed at $\phi = 20$ and 23 d, which is marked with a phase of $\phi = 22$ d in the figure. The identification of the spectral features was done following Howell (2017) and Quimby et al. (2018). Until the maximum light, the spectra of SN 2017gci show a hot blue continuum whose blackbody temperature reaches $T_{\rm BB} \simeq 12000$–14000 K in the spectra about the maximum luminosity. On the redder side of the spectra, the broad Na ID $\lambda\lambda$ 5890, 5896 doublet, the C II $\lambda\lambda$ 6580, 7121 lines and the O I λ 7774 are evident. Tentatively we also identified the Si II λ 6355 feature. At shorter wavelengths, the doublet H&K of the Ca II and the W-shaped O II features at $\lambda\lambda$ 4115, 4357, 4650 are also present. To test their identification, we compared the pre-maximum spectrum of SN 2017gci at $\phi = -7$ d with two synthetic spectra computed with TARDIS (Temperature And Radiative Diffusion In
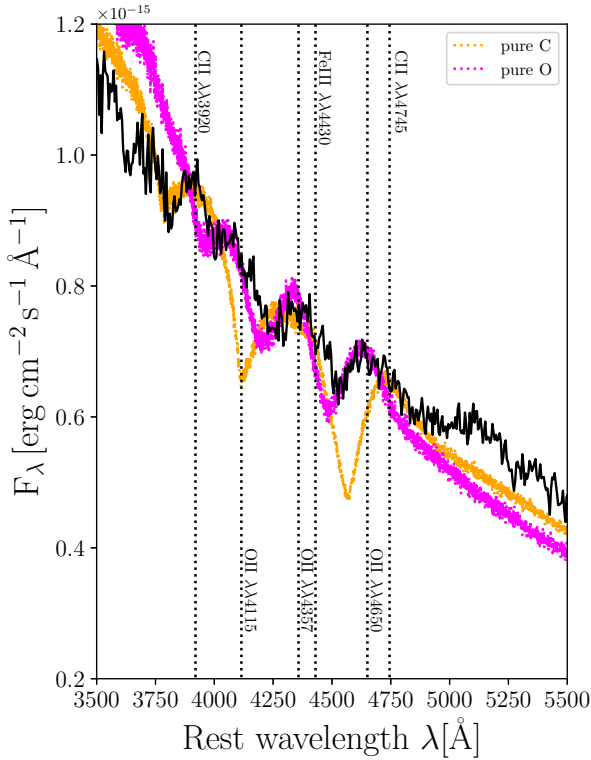
Figure 6. The spectral range between 3500 and 5000 Å; the black solid line is the spectrum of SN 2017gci with rest-frame phase $\phi = -7$ d. The dotted black lines mark the spectral lines, which they are labelled with Ca II, O II, C II, and Fe III, respectively. The orange and the magenta dotted lines trace the synthetic profiles for a pure Carbon and Oxygen composition, respectively, computed with TARDIS. For the sake of completeness, we reported also H&K Ca II doublet, not present in the TARDIS spectrum. The O II features are pretty well matched by the magenta profile.

Supernovae, Kerzendorf & Sim 2014), an open-source, Monte Carlo-based, radiative-transfer spectral synthesis code for SN spectra. The first TARDIS spectrum (see Fig. 6, orange dots) was calculated assuming a pure Carbon chemical abundance while in the second one (magenta dots) a pure Oxygen abundance was input. Both of them assume Local Thermodynamic Equilibrium conditions. As shown in Fig. 6, the features at $\lambda\lambda$ 4115, 4651 are well matched by the pure-O spectrum, but we cannot exclude a line blending with C II spectral features. Moreover, we identified two absorptions as the contribution of Fe II + Fe III. The latter is a common feature among the slow SLSNe I (Inserra 2019).

After ~20 d, the continuum becomes significantly redder with much less prominent O II absorptions. In their place, the Fe II and Mg II features start to be visible. From $\phi \gtrsim 33$ d, the spectra of SN 2017gci resemble those of a Type Ic BL SN at maximum luminosity, as expected by a SLSN I (Pastorello et al. 2010). Then, up to $\phi \sim 156$ there are no significant changes in the the spectra, except for the continuum becoming even fainter and redder. Surprisingly, at $\phi \sim 51$ d a spectral feature consistent with Hα emerges in the spectra and remains visible until $\phi \sim 133$ d. The occurrence of such a feature precedes (~3−6 d) an LC knee (see Section 2.3).

For $\phi \geq 155$ d, the spectra becomes 'pseudonebular' (Nicholl et al. 2019) where emission features start to prevail on the absorption but with a residual fainter continuum. At these epochs, the SN ejecta were cool enough to favour the recombination of the electrons. This reduces the free-electrons density, hence the optical depth and allow

us to investigate the deepest emitting regions of the SN explosion. Moreover, in such a low-density environment the semiforbidden and forbidden atomic transitions start to dominate the spectra. In fact, the emissions of the semiforbidden $\lambda 4571$ Mg I], the [O I] doublet at $\lambda\lambda$ 6300, 6364 and $\lambda\lambda$ 7291, 7323 [Ca II] are present, as well as the strong NIR Ca II $\lambda\lambda$ 8498, 8542, 8662 triplet.

Finally, in the late spectra (at $\phi > 130$ d) of SN 2017gci the narrow Hα- and [O III]-emission lines from the host galaxy become gradually visible. Using these features, we calculated the redshift of the host galaxy, which turns out to be $z = 0.0873 \pm 0.0003$ (where the uncertainty is derived from the dispersion of the measurements). Moreover, the spectrum at $\phi = 187$ d presents two features between 9000 and 11000 Å (see the insert in Fig. 5) where the contribution of Mg II $\lambda 0.92\,\mu$m and $\lambda 1.09\,\mu$m He I might be involved. He I is not frequently seen among SLSNe I, except in the case of PTF10hgi (Quimby et al. 2018) and possibly in the case of SN 2012il (Inserra et al. 2013; Quimby et al. 2018). Further, interpretation of the spectrum at $\phi = 187$ d will be provided in Section 4.4. In the spectrum taken at $\phi = 367$ d, almost all the broad features present in the previous spectrum are no longer present except a residual contribution from [O I]. The NIR part of this spectrum was too faint to be extracted.

3.2.1 *Photospheric velocity*

To estimate the photospheric velocity, we measured the wavelengths corresponding to the minima of the P-Cygni profiles which occur in the spectra of SN 2017gci. They were determined with a Gaussian fit of the absorption features (see Fig. 7) after having been normalized and continuum-subtracted. We performed these measurements from $\phi = -7$ to -4 d, when the O II absorption minima are present in the spectra. Errorbars are estimated by changing the continuum level multiple times before performing the fit. The Doppler shift measured with respect to the rest-frame wavelength of the emissions corresponds to a photospheric velocity v(O II) $\lesssim 8000$ km s^{-1} (see Fig. 7).

4 DISCUSSION

In the following, we will discuss the interpretation of the data presented in the previous sections.

4.1 Metallicity of the host galaxy

We estimated the metallicity of the SN 2017gci site by means of the narrow emission lines of the spectra at $\phi = 187, 367$ d, attributed to the host-galaxy contribution. To test simultaneously several metallicity diagnostics, we used the python-based tool PYMCZ (Bianco et al. 2016). PYMCZ takes as input a list of flux measurements with an associated uncertainty for [O II] $\lambda 3727$, Hβ, [O III] $\lambda 4959$, [O III] $\lambda 5007$, Hα, [N II] $\lambda 6584$, [S II] $\lambda 6717$. For each flux measurement, PYMCZ generates a set of synthetic data via a Monte Carlo simulation. Hence, a Gaussian probability distribution is drawn (whose mean is the input flux and whose standard deviation is the uncertainty of the flux) and randomly sampled. These flux measurements are used to compute the $12 + \log_{10}$(O/H) index via the D02 (De Nicoló et al. 2002), PP04 N2Ha, PP04 O3N2 (Pettini & Pagel 2004), M08 N2Ha, M08 O3O2 (Maiolino et al. 2008) and M13 N2 (Marino et al. 2013) calibrators. The resulting $12 + \log_{10}$(O/H) estimates (see the boxplot in Fig. 8) cluster around ~8.1 (~ 0.3 $Z_\odot$), thus pointing towards a low-metallicity environment as it is expected by the host galaxies
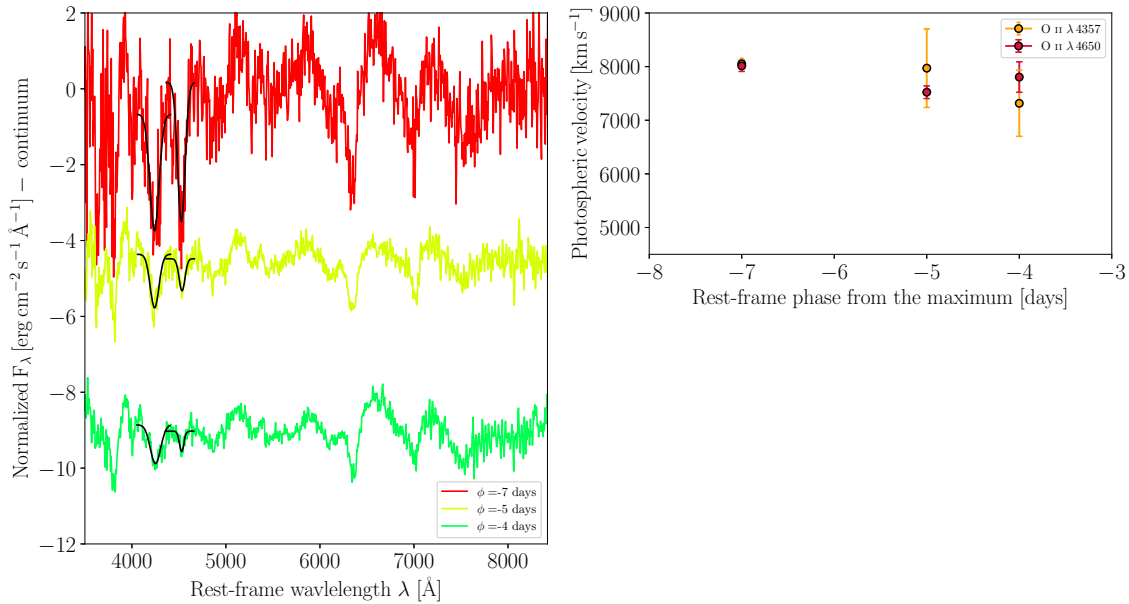
Figure 7. Left-hand panel: normalized and continuum-subtracted spectra between $\phi = -7$ and -4 d. The O II absorption minima were fitted with a Gaussian (black solid lines). Right-hand panel: photospheric velocities retrieved by the absorption minima of the O II (λ4357, 4650) features.

of SLSNe I (see Introduction). A comparison of the PP04 O3O2 metallicity measurements of SN 2017gci with other SLSNe I and GRBs at redshift $z \lesssim 0.1$ is reported in Tab. A13. The environment of SN 2017gci is among those with the lower metallicity.

4.2 [O I] emission profile

In the spectrum of SN 2017gci at $\phi = 187$ d, a close look to the profile of the [O I] $\lambda\lambda$ 6300, 6364 emission doublet points out the presence of a double peak on its topside (see Fig. 9, top panel). The bluest hump of the [O I] doublet peaks at $\lambda \sim 6260$ Å (i.e. $\sim$40 Å blueshifted with respect to its rest-frame wavelength) while the reddest hump peaks between $\lambda \sim 6300$–6310 Å. The 40–50-Å separation between the two peaks (which is lower than the natural 64-Å separation of the doublet) is similar to what was found by Milisavljevic et al. (2010) for the velocity shifts measured on the asymmetric [O I] profiles of a sample of stripped-envelope SNe. In fact, double or multipeaked [O I] profiles were also observed in the late spectra of SNe Ib/c, as in the case of SN 2005bf (Anupama et al. 2005) or SN 2009jf (Sahu et al. 2011; Valenti et al. 2011) (see also Taubenberger et al. 2009, for further studies on the asymmetric [O I] profiles).

The $\sim$40 Å wavelength shift of the blue peak corresponds to a velocity blueshift of $\sim 2000\,\mathrm{km\,s^{-1}}$. To test whether the observed double-peaked [O I] profile could be reproduced by two velocity components, we fitted a composite model made of five Gaussians (see Fig. 9, lower panel): two Gaussians for the $2000\,\mathrm{km\,s^{-1}}$-blueshifted [O I]-doublet component [with a full width at half-maximum (FWHM) of $\sim 4000\,\mathrm{km\,s^{-1}}$], two Gaussians for the rest-frame [O I]-doublet component (with an FWHM of $\sim 4000\,\mathrm{km\,s^{-1}}$) and a broader (FWHM $\sim 11000\,\mathrm{km\,s^{-1}}$) rest-frame component. The FWHM of the two doublets was kept constant in the fitting procedure. The peaks of two couples of Gaussians have a fixed separation of 64 Å and a flux ratio 3:1 (see Fig. 9, lower panel). The broad component was added to better fit the broad wings of the emission feature. The best-fitting curve (see Fig. 9, lower panel) underestimates the flux

emitted in the blue hump of the doublet, but broadly accounts for the 40–50-Å separation of the two peaks.

The physical interpretation of the such profiles is not unique. It was suggested (Taubenberger et al. 2009; Valenti et al. 2011) that they may be the signature of a certain degree of ejecta asphericity. In fact, an asymmetric jet-like explosion (where the major part of the material is launched in the direction opposite to the observer) or ejecta blobs could be responsible of the two velocity components. In addition, the wings could be explained by a more spherically symmetric ejecta component.

Finally, further clues on the ejecta geometry of SN 2017gci will be given by polarimetric observations. In fact, continuum polarization measurements of SN 2017gci display an evolution in the polarization degree, which grows for $\phi > 27$ d. This may be an evidence of the SN photosphere departure from spherical symmetry at late phases (Cikota et al., in preparation).

4.3 Comparisons with other SLSNe I

4.3.1 Comparing the bolometric light curves

We compared the bolometric LC of SN 2017gci with those of a sample of SLSNe I. Among these, the slow-SLSNe I subsample consists of SN 2015bn (Nicholl et al. 2016a, b), PTF12dam (Nicholl et al. 2013; Chen et al. 2015; Vreeswijk et al. 2017), SN 2007bi (Gal-Yam et al. 2009), PTF09cnd (Quimby et al. 2018), SN 2018bsz (Anderson et al. 2018), and LSQ14an (Inserra et al. 2017), whereas the fast subsample includes SN 2011ke and PTF11rks (Inserra et al. 2013) (see Fig. 10). The apparent magnitudes of the last two were taken from The Open Supernova Catalog (https://sne.space/, Guillochon et al. 2017). Soon after the maximum luminosity, the LC decline of SN 2017gci is much faster than the slow SLSNe, except for SN 2015bn which shows an initial change of slope after the maximum luminosity. This might suggest that SN 2017gci is a fast SLSN I, as confirmed by the comparison with SN 2011ke and PTF11rks which fairly well reproduce the decline of SN 2017gci.
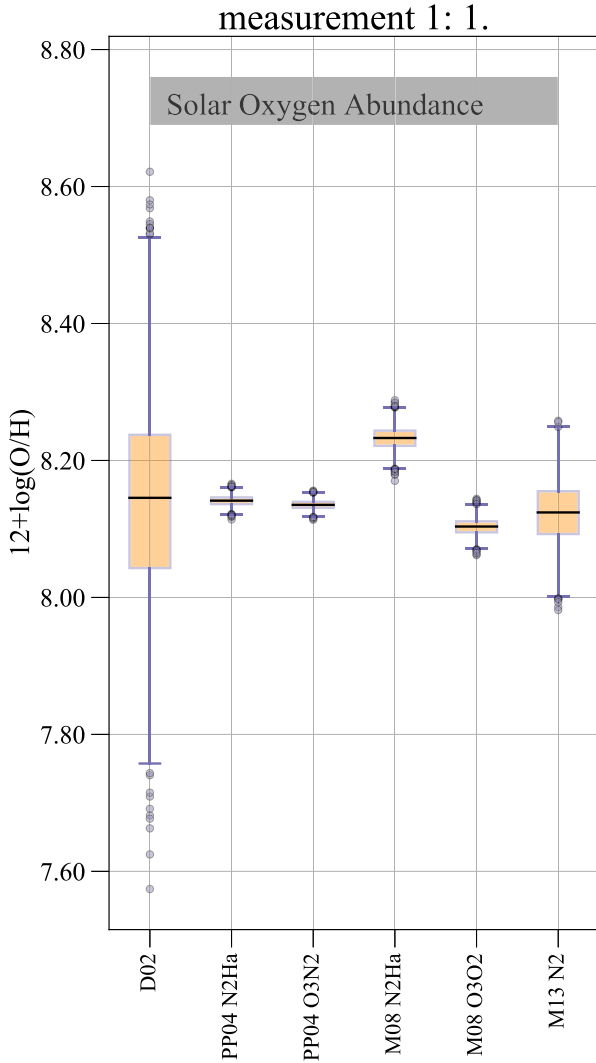
measurement 1: 1.

Solar Oxygen Abundance

Figure 8. A comparison of six metallicity estimates at the location of SN 2017gci. Around the nominal metallicity value (black horizontal lines) synthetic data were generated. The orange box reproduce the interquartile ranges (IQRs), and the blue dots are considered outliers since they deviate from the first and third quartile more then $1.5 \times$ IQR. The grey box spans over the range of the commonly used value for the solar oxygen abundance.

4.3.2 Spectroscopic comparison

Moreover, three spectra of SN 2017gci (at $\phi = -7, 51, 133$ d) have been compared with the spectra of other SLSNe I (see Fig. 11). To the previous comparison sample, we added also two spectra of the intermediate-evolving type I SLSN Gaia16apd (Kangas et al. 2017). At premaximum/premaximum epochs the spectral features of SN 2017gci show similarities with those of two slow SLSNe I, namely SN 2015bn and SN 2018bsz (Anderson et al. 2018). In particular, the presence of the broad C II features on the red side of the spectrum makes SN 2017gci look like a slow SLSN I.

At later phases, the spectra become more similar each other. After ∼40 d from maximum light, the spectra show several broad features and nearly reproduce the overall spectral behaviour of SNe Ic BL at maximum luminosity. This actually holds true both for the slow and fast-evolving SLSNe I (whose prototype is SN 2011ke). Similarly, for $\phi \gtrsim 100$ d, the spectrum of SN 2017gci has characteristics similar to the other SLSNe of the sample, with the presence of Mg I], [Ca II]
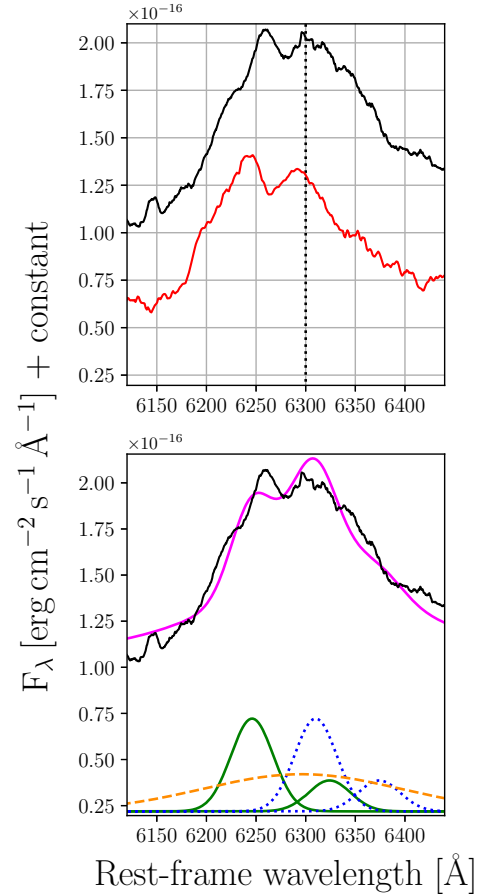

Figure 9. Upper panel: comparison of the asymmetric [O I] λλ 6300, 6364 emission from the spectrum at a rest-frame phase $\phi = 187$ d of SN 2017gci (black solid line) with the same feature shown by the spectrum of the Type Ib SN 2005bf at $\phi = 213$ d (red solid line). Lower panel: fit of a composite model (magenta solid line plotted over the observed spectrum) made by five Gaussians. A couple of 64-Å-separated Gaussians, one at nearly zero velocity (blue dotted line), a couple of Gaussian blueshifted of ∼ 2000 km s^{-1} with respect to the rest-frame doublet (green solid line) and a broad component which peaks at λ ∼ 6300 Å (yellow dashed line).

and the O I emissions. As already mentioned, the resemblance of the late ($\phi \gg 50$ d) post-maximum spectra of SN 2017gci with those of a SN Ic BL was verified via the GEneric cLAssification TOol (GELATO, Harutyunyan et al. 2008) which, for the spectra at $\phi = 51, 133$ d, respectively outputs as best-match template SN 2005az (a Type Ic SN, $\phi = 1$ d) and SN 1997ef (a type Ic BL SN, at $\phi = 41$ d in Fig. 12). In particular, the remarkable similarity of the spectrum of SN 2017gci with that one of SN 1997ef implies that they share the same chemical composition and kinematic.

4.3.3 Temperature evolution

Fig. 13 shows the temporal evolution of the blackbody temperature T_{BB} deduced by fitting the SED with a blackbody curve. From the comparisons between SED and spectra, we estimated that the maximum error introduced by deriving the BB temperature from the SED alone is about 1500 K. We see that at about 50 d after the maximum light the temporal evolution of T_{BB} settles on a plateau of ∼4000–6000 K. This behaviour is similar to the flattening reached at ∼6000–8000 K by the evolution of the blackbody temperature of
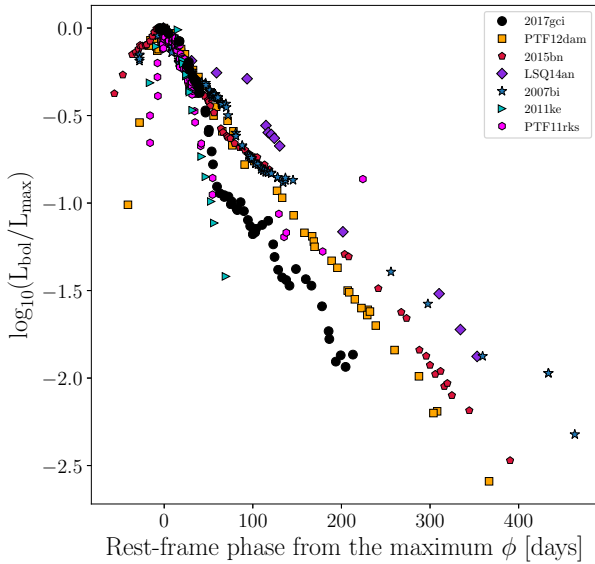
Figure 10. Comparison of the bolometric LC of SN 2017gci (black dots) with those of SN 2015bn (red pentagons), PTF12dam (orange squares), SN 2007bi (purple stars), 2011ke (cyan triangles), and PTF11rks (magenta hexagons).

other SLSNe (e.g. SN 2015bn and SN 2011ke, see Fig. 13 and fig. 13 in Inserra et al. 2013). Nicholl, Guillochon & Berger (2017) proposed that such a temperature floor might be due to O II recombination or to the instability-driven fragmentation of a dense shell. In the case of SN 2017gci, this happens around the same epoch of the knee ($\sim$55−60 d). Therefore, we disfavour the possibility that the O II recombination might be responsible of this temperature levelling since in the O II $\lambda\lambda$ 4115, 4357, 4650 features already disappeared at $\phi = 22$ d.

4.4 Modelling the photometric evolution of SN 2017gci

In order to explain the photometric evolution of SN 2017gci, we considered three possible power sources: the ^{56}Ni decay, the spin-down radiation from a central highly magnetized neutron star (i.e. a newly born magnetar), and the SN ejecta–CSM interaction. We explored the possible contribution from these different power sources under the assumption that the presence of the late LC bumps is to be attributed to the interaction of the SN ejecta with CSM shells or clumps and, following the approach illustrated in Section 2.3, we excluded such bumps when fitting the different models.

Both the ^{56}Ni decay- and the magnetar-powered synthetic LCs were computed via the semi-analytic diffusion scheme described in Inserra et al. (2013, hereafter I13), whose formalism was introduced by Arnett (1982). This scheme relies upon three fundamental assumptions as follows:

(i) the input-power source is centrally located and the ejecta expand in a homologous, spherically symmetric way;
(ii) the opacity κ is independent of time, density ρ, and temperature T;
(iii) radiation-dominated conditions of the environment, hence the radiation pressure $P_{\rm rad}$ is such that

$$P \simeq P_{\rm rad} = \frac{1}{3}aT^4, \tag{1}$$

where P is the total pressure and $a = 7.5646 \times 10^{15}\,{\rm erg\,cm^{-3}\,K^{-4}}$ is the radiation–density constant.

The instantaneous energy balance of such a physical system can be described by the first law of thermodynamics differentiated with respect to time:

$$\dot{U} - \frac{P}{\rho^2}\dot{\rho} = \epsilon - \frac{\partial L}{\partial m}, \tag{2}$$

where U is the internal energy per unit mass and the dot notation indicates the time derivative. The right-hand side of (2) represents the heat-exchange variation, expressed as the sum of the specific input power ϵ and the luminosity radiated away per unit mass, $-\partial L/\partial m$. Here, L is expressed in diffusion approximation:

$$L = \frac{4\pi c r^2}{3\kappa\rho}\frac{\partial a T^4}{\partial r}, \tag{3}$$

where c is the speed of light. Under these assumptions, an LC model is then obtained as a particular solution of (2), substituting for ϵ either the power per unit mass from the ^{56}Ni decay:

$$^{56}{\rm Ni} \rightarrow\, ^{56}{\rm Co} \rightarrow\, ^{56}{\rm Fe}, \tag{4}$$

or the magnetar spin-down luminosity divided by the ejecta mass.

Following the above prescription, we first performed a pure-^{56}Ni-powered fit and found a best-fitting LC profile that cannot reproduce the data and, most importantly, a ^{56}Ni mass even greater than the total ejecta mass. This is, as expected, a non-viable choice to explain the bolometric LC of SN 2017gci, therefore we excluded this possibility.

Then, we considered a magnetar power source (Fig. 14), with the physical parameters of the fit being the ejecta mass $M_{\rm ejecta}$, the polar magnetic field $B_{\rm p}$, the initial orbital period of the magnetar $P_{\rm initial}$, the phase from the maximum luminosity epoch ϕ_0, and the effective opacity κ. In Table A14, we report the best-fitting magnetar model parameters ('MF1'), including a rise time of $\approx$16 rest-frame d, consistent with the fast-evolving interpretation (Inserra 2019).

While the best-fitting magnetar model is able to describe the maximum luminosity of SN 2017gci, it does not entirely explain the behaviour of the observed bolometric LC at later times. In particular, between about 100 and 200 d, the observed luminosity is significantly higher and requires an additional power source. As discussed below, this could be the interaction of the ejecta with CSM clumps.

The above result depends on the exclusion from the fitting procedure of data points in two different intervals between about 100 and 200 d (see Fig. 3). In order to provide also a more conservative indication, we explored in full the admissible parameter range for a magnetar LC in presence of all data points (shaded region in Fig. 14). We found that the observed bolometric LC could not be easily described by the magnetar scenario solely outside the following ranges: $3.5 \times 10^{14} \lesssim B_{\rm p} \lesssim 8 \times 10^{14}$ G, $1 \lesssim P_{\rm initial} \lesssim 5$ ms, $7.7 \lesssim M_{\rm ejecta} \lesssim 12\,{\rm M}_{\odot}$, $0.08 \lesssim \kappa \lesssim 0.2\,{\rm cm^2\,g^{-1}}$, and $18 \lesssim \phi_0 \lesssim 30$ d.

Finally, we considered the SN ejecta–CSM interaction as the main power source for the bolometric LC, in particular at maximum luminosity. To fit such a model, we used TIGERFIT. Since TIGERFIT works at fixed phase from the explosion ϕ_0, we assumed different values for it between 18 and 30 d. TIGERFIT embeds the modules csm0 and csm2, which refer to the case of a steady-state wind and a constant-density CSM shell, respectively.[9] Using both modules and fitting only up to the knee (at about 54–57 d), we found the best

---

[9]The two modules are labelled with the value of the exponent s of the density-profile slope $\rho_{\rm CSM} \propto r^{-s}$. Hence, $s = 2$ corresponds to a wind solution and $s = 0$ to a constant–density shell.
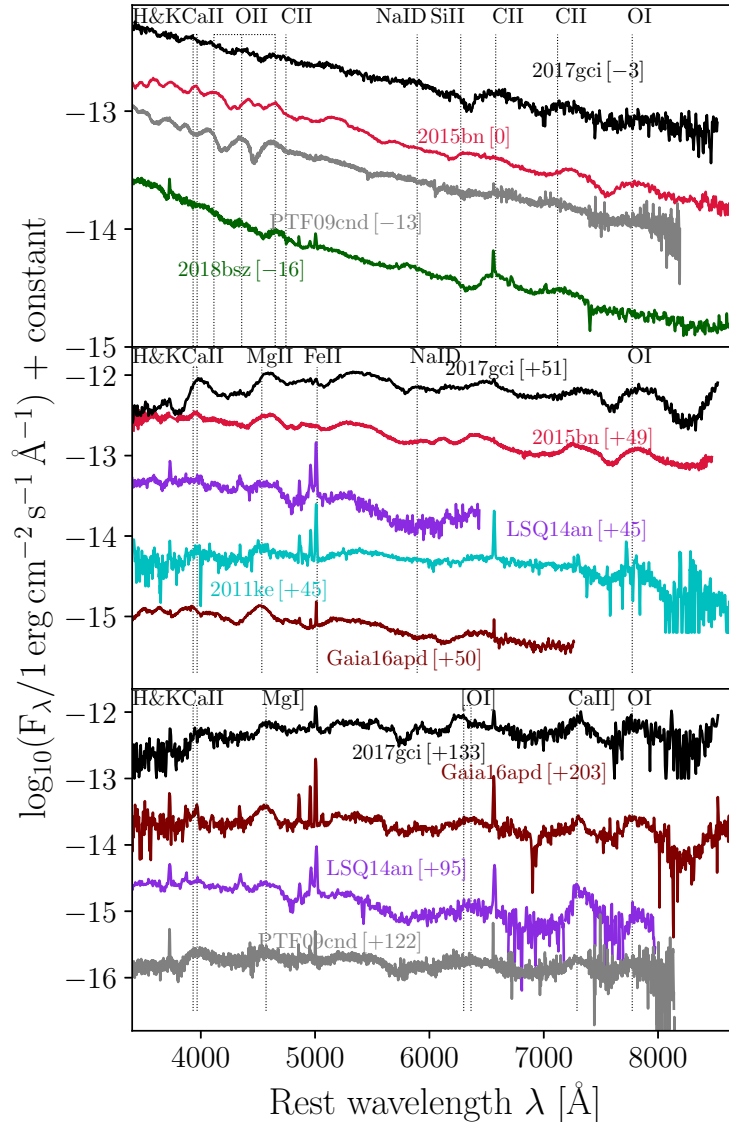
Figure 11. Comparisons of three spectra of SN 2017gci (black line) with other SLSNe I spectra at different phases with respect to the maximum luminosity epoch. Each spectrum is identified by the name of the SLSN I and its rest-frame phase from the maximum light (in square brackets), and the labels are coloured as the spectrum they refer to. Line-identifications (black dotted lines) are also provided. Top panel: SLSN I spectra at premaximum and maximum. Middle panel: SLSN I spectra about 40 d after the maximum. Bottom panel: SLSN I spectra at late phases ($\gtrsim$ 100 d) after the maximum-luminosity epoch. The spectra of PTF09cnd (Quimby et al. 2018), SN 2018bsz (Anderson et al. 2018), Gaia16apd (Kangas et al. 2017), and LSQ14an (Inserra et al. 2017) were taken from The Open Supernova Catalogue. For the spectra of SN 2011ke (middle panel) and of SN 2017gci at $\phi = 133$ (bottom panel), the narrow emissions lines from the host galaxy were cut for display purposes.

agreement with the csm0 model for $\phi_0 = 30$ d. This gives a CSM mass of 4.9 $M_\odot$, for a progenitor radius $R_{progenitor} \simeq 0.004 \times 10^{14}$ cm (see Table A14 for further details). As shown in Fig. 14 (green dashed profile, referring to $\phi_0 = 30$ d), this model is able to reproduce the maximum luminosity of SN 2017gci, although any data point after the knee require an additional power source. Overall, we conclude that the maximum and initial part of the LC could be explained with a magnetar power source or with the ejecta–CSM interaction.

As mentioned above, we assumed that the luminosity undulations observed between the knee and $\phi \simeq 200$ d can be explained via the interaction of the ejecta with CSM clumps. This appears to be the most natural explanation of the bumps in the LCs of SLSNe I (Moriya, Sorokina & Chevalier 2018). Following Nicholl et al. (2016a), we attempted an estimate of the mass of the CSM clumps

M_{CSM} based on the simple relation

$$E_{rad} \simeq \frac{1}{2} M_{CSM} u_{ej-CSM}^2 , \qquad (5)$$

where E_{rad} is the energy radiated at the epochs of the LC bumps and u_{ej-CSM} is the relative velocity between the ejecta and the CSM clumps. Taking our best-fitting magnetar model as a reference, E_{rad} was computed by integrating the difference between the bolometric LC and the magnetar fit between $\phi = 101$ and 130 d for the first bump and between $\phi = 138$ and 196 d for the second one. We obtained $E_{rad, 1} \simeq 3.5 \times 10^{48}$ erg and $E_{rad, 2} \simeq 2.8 \times 10^{48}$ erg. Then, assuming that the CSM has a negligible velocity compared to the ejecta, we
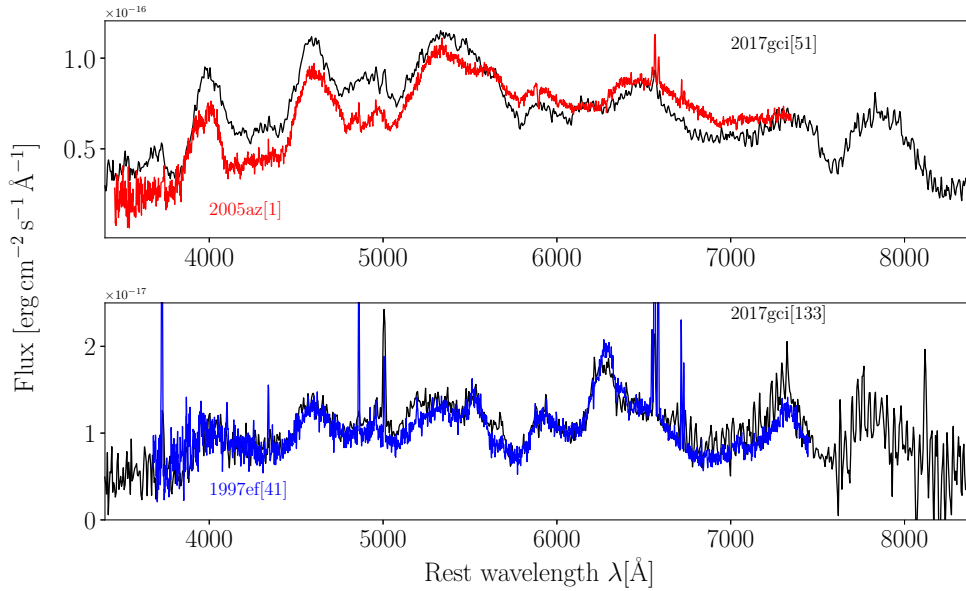
Figure 12. Spectral comparisons of SN 2017gci obtained with the tool GELATO. The SN name is labelled in the plot alongside the rest-frame phase ϕ with respect to the maximum light (in square brackets). Top panel: SN 2017gci (black, $\phi = 51$ d) with the spectrum of the Type Ic SN 2005az (red, $\phi = 1$ d). Bottom panel: SN 2017gci (black, $\phi = 135$ d) with the spectrum of the type Ic BL SN 1997ef (blue, $\phi = 41$ d).
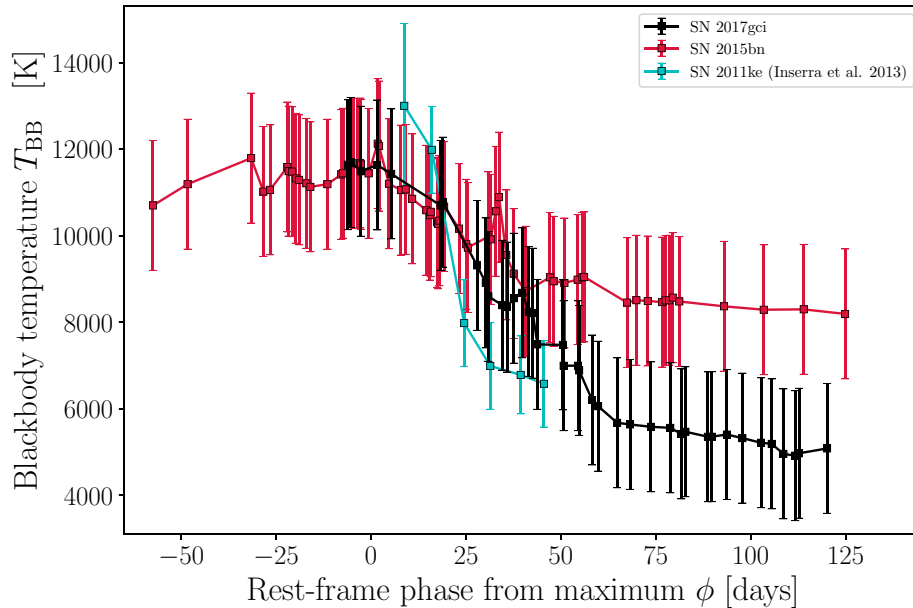
Figure 13. Temporal evolution of the black-body temperature of SN 2017gci (black squares), SN 2015bn (red squares), and SN 2011ke (cyan squares). The blackbody temperatures for both SN 2017gci and SN 2015bn were retrieved by a blackbody fit of the SED, while the temperatures of SN 2011ke are taken from Inserra et al. (2013).

have

$$M_{\text{CSM},1} \simeq 5.5 \times 10^{-3} \left(\frac{u_{\text{ejecta}}}{8000 \, \text{km s}^{-1}} \right)^{-2} M_\odot \tag{6}$$

and

$$M_{\text{CSM},2} \simeq 4.4 \times 10^{-3} \left(\frac{u_{\text{ejecta}}}{8000 \, \text{km s}^{-1}} \right)^{-2} M_\odot . \tag{7}$$

The interaction postulated between the SN ejecta and the CSM clumps may possibly leave its signature in the optical spectra (like the presence of narrow emission lines). However, the spectrum at phase $\phi = 103$ d (nearly corresponding to a bump) does not show any sudden difference compared to the subsequent one (at $\phi = 133$ d, which is about a minimum of the LC undulations). This can be understood also from the undulations in Fig. 4, which do not show a noticeable wavelength dependence in optical bands, suggesting that in this case the hypothetical CSM interaction had a grey effect on the opacity of SN 2017gci.

In addition, if the spectral feature at about $\lambda \sim 6520$ Å (see Section 3.2) is indeed Hα, it could be a signature that the interaction
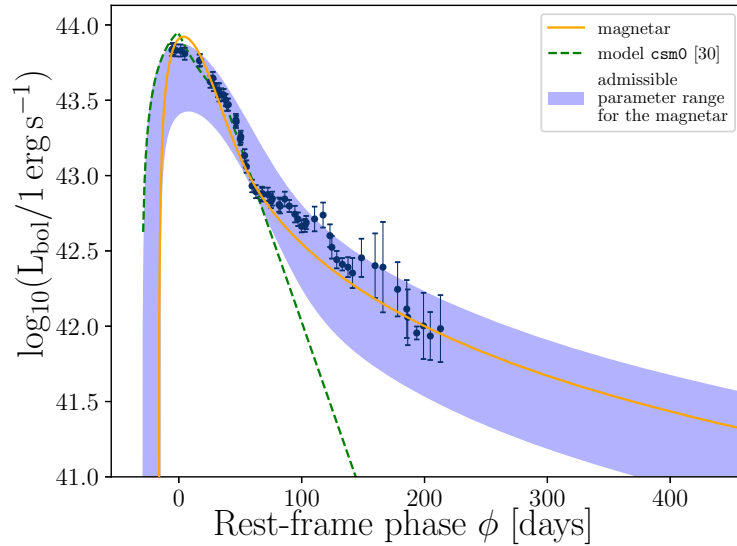
Figure 14. Pseudo-bolometric LC of SN 2017gci compared with a magnetar-powered LC fit (yellow line), a constant–density CSM shell model obtained with TIGERFIT (green dashed line) assuming a phase from the explosion ϕ_0 of 30 d. In addition, the blue-shaded area covers the admissible parameter range for a magnetar model fit.

with a hydrogen-rich CSM has started already before the knee: this could account for the almost linear decline of the LC (see Section 3), thus supporting the idea that the bumps are caused by overdensities in the CSM. This is also supported by the fact that the Hα-like feature apparently disappears from the spectrum at $\phi = 133$ d which is consistent with the disappearing of the first bump (see Fig. 15). Hence, the second bump could be the signature of a hydrogen-poor clump of CSM, although this would require the presence of CSM clumps with very different chemistry.

4.5 SN 2017gci at nebular phases

We compared the spectrum of SN 2017gci at $\phi = 187$ d thanks to spectral-modelling numerical code SUMO (Jerkstrand et al. 2011, 2012, 2017). The publicly-available[10] SUMO models for SLSNe I (Jerkstrand et al. 2017) are computed at 400 d after the explosion, at a constant ejecta velocity $v_{ejecta} = 8000$ km s^{-1} and with $N = 100$ random clumps for different ejecta compositions,[11] ejecta masses M_{ejecta}, energy deposition E_{dep} and filling factors[12] f. Before adapting a SUMO solution to the observed spectrum at $\phi = 187$ d, we estimated the residual contribution of the host galaxy emission therein, similarly to Jerkstrand et al. (2017, see their Section 2). Since a spectrum of the host galaxy is not available, we took a starbust-galaxy template spectrum from the sample of Calzetti, Kinney & Storchi-Bergmann (1994), which was obtained by averaging over a sample of starbust galaxies with $0.11 < E(B - V) < 0.21$ mag. Then we scaled the template spectrum on the SED of the host galaxy, which we measured from the template images (see Section 2). Hence, we subtracted the scaled template spectrum to the XS spectrum at $\phi = 187$ d (see Fig. 16). We found that

---

[10]https://star.pst.qub.ac.uk/wiki/doku.php/users/ajerkstrand/start/

[11]Pure Oxygen, C-burning ashes, Oxygen (92 per cent), and Magnesium (8 per cent).

[12]The filling factor f expresses the percentage volume of clumps. Hence, $1 - f$ corresponds to vacuum.

the [O I] $\lambda\lambda$ 6300, 6364 is well reproduced by the spectral models computed with C-burning composition (O/Mg/Ne dominated) with $M_{ejecta} = 10$ M$_\odot$, $N_{clumps} = 100$, $f = 0.001$ with an energy deposition $E_{dep} = 5 \times 10^{41}$ or 2×10^{42} erg s^{-1} (see Fig. 16). The latter were scaled by a factor of 2 (see the caption of Fig. 16) to roughly fit the luminosity of the spectrum. The ejecta-mass value of the two models is fairly similar to the one obtained from the fit of the magnetar-powered synthetic LC (see Tab. A14) as well as the magnetar energy deposition, which in MF1 is $\sim 9.44 \times 10^{41}$ erg s^{-1} for $\phi = 187$ d.

Moreover, for both the two models, we showed the effect of increasing the filling factor. The luminosities of the Mg I] λ4571 and Mg I λ15400 suggest that the ejecta are likely clumped with a filling factor $f \ll 1$ (Jerkstrand et al. 2017). This would not be surprising in both the magnetar and in the CSM-interaction scenario, where the SN ejecta are piled up by the pulsar-wind bubble in a high-density layer which is afterwards broken up by hydrodynamical instabilities. However, if such a thin dense shell survived (like in one-dimensional simulations, see e.g. fig. 2 in Kasen & Bildsten 2010), it would result in a clear observational signature like, e.g. boxy-shaped spectral lines (see Wheeler et al. 2000) which we do not observe in the case of SN 2017gci. Recent two-dimensional hydrodynamic simulations of a magnetar-driven SLSN explosion (Chen, Woosley & Sukhbold 2016) predict indeed that the low-density bubble inflated by the magnetar spin-down radiation becomes unstable to the onset of Rayleigh–Taylor Instabilities after the collision with the high-density SN ejecta. From a physical point of view, increasing the ejecta clumpiness enhances the effect of trace elements on temperature and ionization. In such a regime, nebular spectra are then more sensitive to the progenitor metallicity. Hence, the features shared by the nebular spectra of SLSNe I with those of Type Ic BL SNe might suggest that they have similar progenitors and/or explosion mechanisms (Nicholl et al. 2016b).

Finally, it is possible to infer a physical-parameter estimate by means of the analytic relations discussed by Jerkstrand et al. (2017). Substituting the luminosity of the Oxygen recombination line lumi-
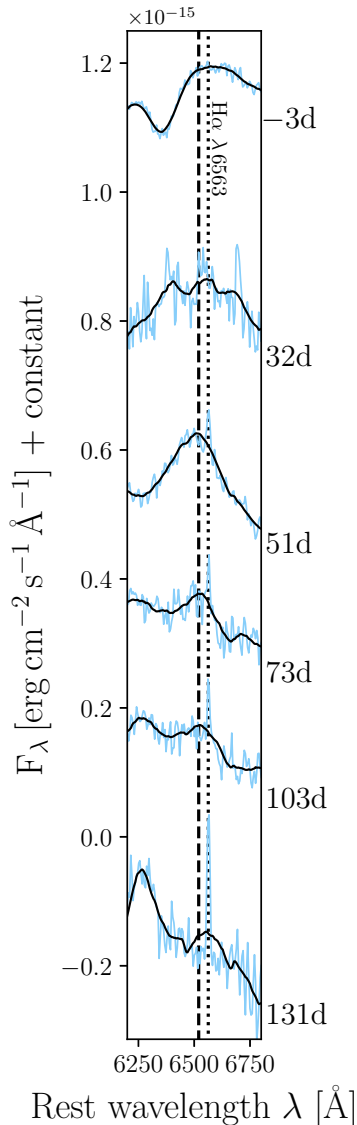
from the intensity ratio of the Ca II NIR triplet and the forbidden [Ca II]. Such a ratio is particularly high in the case of the spectrum of SN 2017gci (at $\phi = 187$ d) since it reaches ~ 2.9. This implies $n_e \gtrsim 1 \times 10^9$ cm^{-3} (for a temperature of 6000–6500 K, see fig. 14 in Jerkstrand et al. 2017). This result is robust with respect to possible O line contaminations to the λ 7300 and λ 8600 features (see Jerkstrand et al. 2017, for details). Such a high density at nebular phases could be achieved in principle by the matter swept-up by the pulsar-wind nebula. Finally, equation (9) from Jerkstrand et al. (2017) provides an estimate of the magnesium mass M_{Mg} via the luminosity emitted within the Mg I 1.5 μm feature, $L_{1.5\mu m} \simeq 6.4 \times 10^{39}$ erg s^{-1} with the following formula:

$$\frac{M_{Mg}}{1\,M_\odot} = \frac{L_{1.5\mu m}}{6.6 \times 10^{38}\,\mathrm{erg\,s^{-1}}} \left(\frac{n_e}{10^8\,\mathrm{cm^{-3}}}\right)^{-1} \left(\frac{\alpha^{eff}(T)}{1 \times 10^{-13}\,\mathrm{cm^3\,s^{-1}}}\right)^{-1}. \quad (9)$$

Using the same value of n_e and with $\alpha^{eff}(T) = 1 \times 10^{-13}$ cm^3 s^{-1}, it gives $M_{Mg} \simeq 1\,M_\odot$. Provided that the Mg mass fraction is typically 5–10 per cent of the O/Mg mass, the result of the equation (9) implies a O/Mg zone mass $\lesssim 10\,M_\odot$. This also supports the choice of the $M_{ejecta} = 10\,M_\odot$ models for SN 2017gci, given that only such a zone mass is consistent with the Mg I 1.5-μm constraint. These results might be in favour of the picture of a quite massive progenitor star ($\gtrsim 40\,M_\odot$, Jerkstrand et al. 2017) for SN 2017gci.

5 CONCLUSIONS

We have presented the UV/optical/NIR photometry and the optical spectra of the nearby SN 2017gci, whose K-corrected absolute magnitude at maximum luminosity in g band is ~ -21.5 mag. Its LC presents a sudden change in the slope (the 'knee') and two bumps at ~ 110 and ~ 160 d after the maximum luminosity. Similar characteristics are not infrequent among the known slow SLSNe I. Its spectroscopic evolution follows the typical one of SLSNe I, which at about 40 d from the maximum light turns into a SN-Ic BL-like spectrum at its maximum luminosity.

We employed a semi-analytical model to fit the bolometric LC, assuming the following power sources: (i) the ^{56}Ni decay chain; (ii) the magnetar-spin-down radiation; and (iii) the ejecta–CSM interaction. The magnetar fit allowed for a physical parameter estimate which envisages an ejecta mass of about $\sim 9\,M_\odot$. This value is similar to those obtained for the SNe Ic BL (as in the case of SN 1997ef, Nakamura et al. 2000). Also, we performed a fit with the tool TIGERFIT assuming that the CSM interaction contributes to the maximum luminosity. This requires a CSM mass of $\sim 5\,M_\odot$ and an ejecta mass of $\sim 12 M_\odot$. In addition, we ascribe the presence of the knee and the bumps to the CSM interaction, which is supported by a likely presence of an almost coeval Hα emission in the spectrum.

Additional indications were obtained from the moderate-resolution XS spectrum at phases $\phi = 187$ d thanks to a handful of spectral models produced via the SUMO single-zone code. We found the best agreement with models assuming $M_{ejecta} = 10\,M_\odot$ and an energy deposition $E_{dep} = 5 \times 10^{41} - 2 \times 10^{42}$ erg s^{-1}. Interestingly, this broadly agrees with the magnetar luminosity of MF1 at the rest-frame phase $\phi = 187$ d is 9.44×10^{41} erg s^{-1}.

Overall, our analysis points towards a progenitor mass of $\gtrsim 40\,M_\odot$ for SN 2017gci.

The spectroscopic similarities between SLSNe I and SNe Ic BL (e.g. SN 1997ef) support the hypothesis that these SN subclasses are linked by a continuum distribution and share a similar origin (Liu et al. 2017; De Cia et al. 2018; Quimby et al. 2018; Gal-Yam 2019; Lin et al. 2020). However, the solution of the SLSN-SN Ic BL puzzle requires both a wider data sample and a further improvement of the modelling tools. In particular, we expect that next-generation surveys
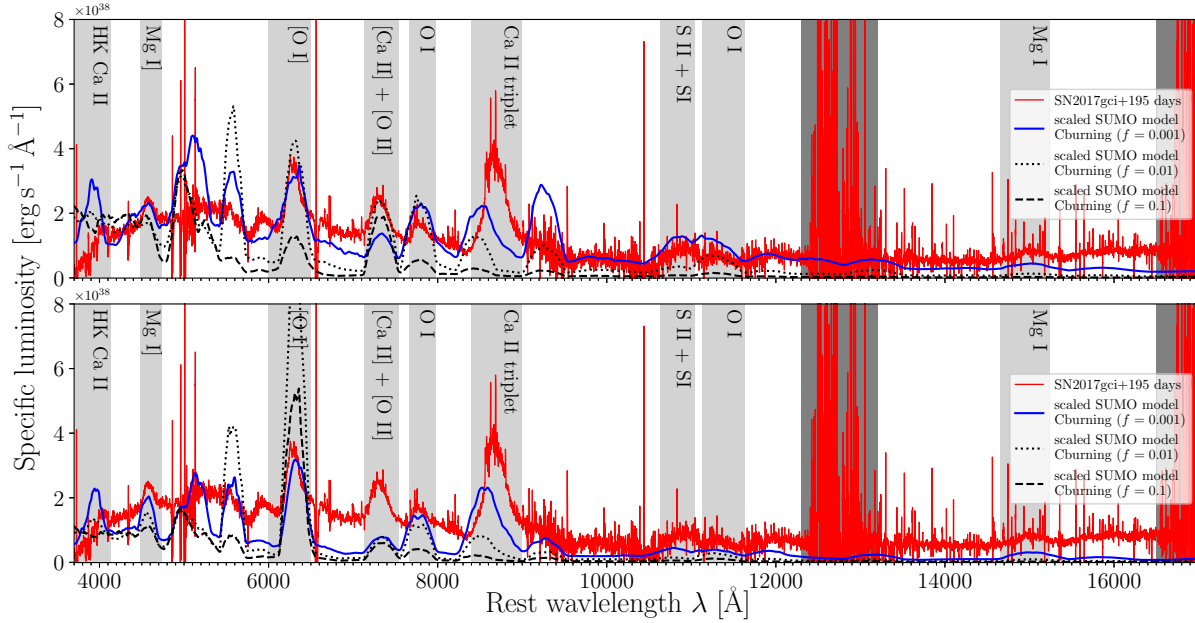

Figure 15. The broad feature around $\lambda \simeq 6520$ Å emerging at $\phi = 51$ d and broadly consistent with Hα. The black dashed line indicates the centroid of the emission and the black dotted lines marks the rest wavelength of the Hα line. Similarly to Fig. 5, the light-blue solid line is the observed spectrum after having subtracted a blackbody continuum. The black solid line is the same but smoothed with a Savitzki–Golay filter. The rest-frame phase is labelled on the right for each continuum-subtracted spectrum.

nosity L_{7774} (for which we measured $L_{7774} = 1.1 \times 10^{40}$ erg s^{-1}), we constrained the electron density n_e as follows:

$$n_e f^{1/2} = 4.20 \times 10^7 \left(\frac{v_{exp}}{8000\,\mathrm{km\,s^{-1}}}\right)^{-3/2} \left(\frac{\alpha^{eff}(T)}{2 \times 10^{-13}\,\mathrm{cm^3\,s^{-1}}}\right)^{-1/2}$$
$$\mathrm{cm^{-3}}, \quad (8)$$

where $\alpha^{eff}(T)$ is the effective recombination rate and v_{exp} is the maximum velocity of the expanding gas, once spherical symmetry is assumed. The value that we obtained for $n_e f^{1/2}$ is in the range outlined by Nicholl et al. (2019) for a sample of 41 spectra of 12 SLSNe (see their fig. 22). Then, assuming a filling factor $f = 0.001$, a rise time of 16 d (as suggested by MF1), $\alpha^{eff}(T) = 2 \times 10^{-13}$ cm^3 s^{-1} and $v_{exp} = 8000$ km s^{-1}, equation (8) implies $n_e \simeq 1.3 \times 10^9$ cm^{-3}. This value agrees with the electron density that can be deduced

Figure 16. Comparison of the spectrum of SN 2017gci at $\phi = 187$ d (red solid line) with the models output by the SUMO code (Jerkstrand et al. 2017, see the text). A residual host contribution was estimated and subtracted to the original one (see text). Upper panel: models with $M_{\rm ejecta} = 10\,{\rm M_\odot}$, energy deposition $E_{\rm dep} = 2 \times 10^{42}$ erg s^{-1}, and $f = 0.001$ (blue solid line), 0.01 (black dotted line) and 0.1 (black dashed line). Lower panel: as before, but with models whose energy deposition is $E_{\rm dep} = 5 \times 10^{41}$ erg s^{-1}. These were scaled by a factor of 2. The light-grey shaded area mark the features of the spectrum, whereas the dark-grey ones are placed in correspondence with the atmospheric corrections of the XS-reduction pipeline (Krühler et al. 2015).

such as the Legacy Survey of Space and Time at the Vera Rubin Observatory will discover a huge number of SLSNe (Villar et al. 2018), which would be crucial especially for very early detections. In addition, three-dimensional hydrodynamical modelling including an improved treatment of radiative transport will allow us to better investigate the properties of SLSNe at both early and late phases, thus boosting our understanding of the underlying explosion mechanism (Soker & Gilkis 2017) as well as the nature of the progenitor stars.

DATA AVAILABILITY STATEMENT

The data presented in this paper and listed in Appendix A are available in the online supplementary material.

REFERENCES

Anderson J. P. et al., 2018, A&A, 620, 67
Anupama G. C., Sahu D. K., Deng J., Nomoto K., Tominaga N., Tanaka M., Mazzali P. A., Prabhu T. P., 2005, ApJ, 631, L125
Arnett W. D., 1982, ApJ, 253, 785
Becker A., 2015, Astrophysics Source Code Library, record ascl:1504.004
Bianco F. B., Modjaz M., Oh S. M., Fierroz D., Liu Y. Q., Kewley L., Graur O., 2016, 16, 54
Brown T. M. et al., 2011, Bull. Am. Astron. Soc., 218, 132.02
Buzzoni B. et al., 1984, The Messenger, 38, 9
Calzetti D., Kinney A. L., Storchi-Bergmann T., 1994, ApJ, 429, 582
Cappellaro E., 2014, SNOOPY: A Package for PSF Fitting and Template Subtraction, Available at: http://sngroup.oapd.inaf.it/snoopy.html
Chambers K. C. et al., 2016, preprint (arXiv:1612.05560)
Chatzopoulos E., Wheeler J. C., Vinko J., 2012, ApJ, 746, 121
Chatzopoulos E., Wheeler J. C., Vinko J., Horvath Z. L., Nagy A., 2013, ApJ, 773, 76
Chen et al., 2018, ApJ, 867, 31
Chen K.-J., Woosley S. E., Sukhbold T., 2016, ApJ, 832, 73
Chen T.-W. et al., 2013, ApJ, 763, L28
Chen T.-W. et al., 2015, MNRAS, 452, 1567
Chen T. W., Smartt S. J., Yates R. M., Nicholl M., Krühler T., Schady P., Dennefeld M., Inserra C., 2017, MNRAS, 470, 3566
Chen T. W. et al., 2017, ApJ, 470, 3566
Chevalier R. A., Fransson C., 2003, 598, 171
Chevalier R. A., Irwin C. M., 2011, ApJ, 729, L6
Chonis T. S., Gaskell C. M., 2008, AJ, 135, 264
Cikota A. et al., 2017, MNRAS, 469, 4705
De Cia A. et al., 2018, ApJ, 860, 100
Delgado A., Harrison D., Hodgkin S., Leeuwen M. V., Rixon G., Yoldas A., 2017, TNSTR, 2017-873, 1
Denicoló G., Terlevich R., Terlevich E., 2002, MNRAS, 330, 69
Dessart L., Waldman R., Livne E., Hillier D. J., Blondin S., 2013, MNRAS, 428, 3227
Elias-Rosa N. et al., 2006, MNRAS, 369, 1880
Fabricant D. et al., 2019, Publ. Astron. Soc. Pac., 131, 075004

Freudling W., Romaniello M., Bramich D. M., Ballester P., Forchi V., García-Dabló C. E., Moehle S., Neese M. J., 2013, A&A, 559, A96
Gaia Collaboration et al., 2016, A&A, 595, A1
Gaia Collaboration et al., 2016, A&A, 595, A2
Gal-Yam, 2019, Annual Review of Astronomy and Astrophysics, 305
Gal-Yam A., 2012, Science, 337, 927
Gal-Yam A. et al., 2009, Nature, 462, 624
Ginzburg S., Balberg S., 2012, ApJ, 757, 178
Greiner J. et al., 2008, Publ. Astron. Soc. Pac., 120, 405
Greiner J. et al., 2015, Nature, 523, 189
Guillochon J., Parrent J., Kelley L. Z., Margutti R., 2017, ApJ, 835, 64
Harutyunyan A., Pfahler P., Pastorello A. et al., 2008, A&A, 488, 383
Howell D. A., 2017, in Alsabti A., Murdin P., eds, Handbook of Supernovae. Springer, p. 431
Inserra C., 2019, Nat. Astron., 3, 697
Inserra C. et al., 2013, ApJ, 770, 128 (I13)
Inserra C. et al., 2017, MNRAS, 468, 4642
Izzo L. et al., 2018, A&A, 610, A11
Jerkstrand A., Fransson C., Kozma C., 2011, A&A, 530, A45
Jerkstrand A., Fransson C., Maguire K., Smartt S., Ergon M., Spyromilio J., 2012, A&A, 546, A28
Jerkstrand A., Smartt S. J., Heger A., 2016, MNRAS, 455, 3207
Jerkstrand A. et al., 2017, ApJ, 835, 13
Kangas T. et al., 2017, MNRAS, 469, 1246
Kasen D., Bildsten L., 2010, ApJ, 717, 245
Kerzendorf W. E., Sim S. A., 2014, MNRAS, 440, 387
Kruehler T. et al., 2015, A&A, 581:A125
Krühler T. et al., 2008, ApJ, 685, 376
Kumar A. et al., 2020, ApJ, 892, 28
Leloudas et al., 2015, MNRAS, 449, 917
Lin W. L., Wang X. F., Wang L. J., Dai Z. G., 2020, ApJ, 903, 24L
Liu, Yu-Q., Modjaz M., Bianco F. B., 2017, ApJ, 845, 85
Lunnan R. et al., 2014, ApJ, 787, 138
Lunnan R. et al., 2018, Nat. Astron., 2, 887
Lunnan R. et al., 2019, ApJ, 901, 19
Lyman J. et al., 2017, The Astronomer's Telegram, 2017-881, 1
Maiolino R. et al., 2008, A&A, 488, 463
Marcote et al., 2020, Nature, 577, 190
Margalit B., Metzger B. D., Thompson T. A., Nicholl M., Sukhbold T., 2018, MNRAS, 475, 2659
Marino R. A. et al., 2013, A&A, 559, A114
Metzger B. D., Vurm I., Hascoet R., Beloborodov A. M., 2014, MNRAS, 437, 703
Milisavljevic D., Fesen R. A., Gerardy C. L., Kirshner R. P., Challis P., 2010, ApJ, 709, 1343
Moorwood A., Cuby J.-G., Lidman C., 1998, The Messenger, 91, 9
Moriya T., Sorokina E. I., Chevalier R. A., 2018, Space Science Reviews
Nakamura T. et al., 2000, in Martens P. C. H., Tsuruta S., Weber M., eds, IAU Symp. 195, Highly Energetic Physical Processes and Mechanisms for Emission from Astrophysical Plasmas. Kluwer, Dordrecht, p. 347
NASA High Energy Astrophysics Science Archive Research Center (HEASARC), 2014, Astrophysics Source Code Library, record ascl:1408.004
Nicholl M., Berger E., Blanchard P. K., Gomez S., Chornock R., 2019, ApJ, 871, 102
Nicholl M., Guillochon J., Berger E., 2017, ApJ, 850, 55
Nicholl M., Williams P. K. G., Berger E., Villar V. A., Alexander K. D., Eftekhari T., Metzger B. D., 2017, ApJ, 843, 84
Nicholl M. et al., 2013, Nature, 502, 346
Nicholl M. et al., 2014, MNRAS, 444, 2096
Nicholl M. et al., 2015, MNRAS, 452, 3869
Nicholl M. et al., 2016a, ApJ, 826, 39
Nicholl M. et al., 2016b, ApJ, 828, L18
Oke J. B. et al., 1995, Publ. Astron. Soc. Pac., 107, 375
Pastorello A. et al., 2010, ApJ, 724, L16
Perley D. A. et al., 2016, ApJ, 830, 13

Pettini M., Pagel B. E. J., 2004, MNRAS, 348, L59

Pignata G. et al., 2004, MNRAS, 355, 178

Poznanski D., Prochaska J. X., Bloom J. S., 2012, MNRAS, 426, 1465

Quimby R. M. et al., 2018, ApJ, 855, 2

Rakavy G., Shaviv G., 1967, ApJ, 148, 803

Ravi V. et al., 2019, Nature, 572, 352

Sahu D. K., Gurugubelli U. K., Anupama G. C., Nomoto K., 2011, MNRAS, 413, 2583

Salgado J., González-Núñez J., Gutiérrez-Sánchez R., Segovia J. C., Durán J., Hernández J. L., Arviset C., 2017, Astronomy and Computing, 21, 22

Schlafly E. F., Finkbeiner D. P., 2011, ApJ, 737, 103

Schulze S. et al., 2018, MNRAS, 473, 1258

Skrutskie M. F. et al., 2006, AJ, 131, 1163

Smartt S. J. et al., 2015, A&A, 579, A40

Smith N. et al., 2007, 666, 1116

Soker N., Gilkis A., 2017, ApJ, 851, 95

Stetson P. B., 1987, Publ. Astron. Soc. Japan, 99, 191

Stritzinger M. et al., 2002, AJ, 124, 2100

Suzuki A., Maeda K., 2017, MNRAS, 466, 2633

Suzuki A., Maeda K., 2019, ApJ, 880, 150

Tanga M., Krühler T., Schady P., Klose S., Graham J. F., Greiner J., Kann D. A., Nardini M., 2018, A&A, 615, A136

Taubenberger S. et al., 2009, MNRAS, 397, 677

Thöne C. C., de Ugarte Postigo A., García-Benito R., Leloudas G., Schulze S., Amorin R., 2015, MNRAS, 451, L65

Thöne C. C. et al., 2014, MNRAS, 441, 2034

Tonry J. L. et al., 2012, ApJ, 750, 99

Valenti S. et al., 2011, MNRAS, 416, 3138

Van Dokkum P. G., 2001, Publ. Astron. Soc. Japan, 113, 1420

Vernet J. et al., 2011, A&A, 536, A10

Villar V. A., Nicholl M., Berger E., 2018, ApJ, 869, 166

Vreeswijk P. M. et al., 2017, ApJ, 835, 58

Wheeler J. C., Piran T., Weinberg S., 1990, Supernovae-Proceedings of the 6th Jerusalem Winter School for Theoretical Physics World Scientific. World Scientific Publishing, Teaneck, NJ

Woosley S. E., 2010, ApJ, 719, L204

Yan L. et al., 2015, ApJ, 814, 108

Yan L. et al., 2017, ApJ, 848, 6

Yoshida T., Umeda H., Maeda K., Ishii T., 2016, MNRAS, 457, 351

APPENDIX A: TABLES

Table A1. $UVW1$, $UVM2$, and $UVW2$ filters observed (non-K-corrected) aperture magnitudes (in AB system). Errors are in parentheses. The full table is available online as supplementary material.

MJD	rf phase from maximum	$UVW1$	$UVM2$	$UVW2$	Instrument
57986.00	−3.96	–	–	19.58(0.08)	*Swift*/UVOT
57986.77	−3.25	–	19.46(0.05)	–	*Swift*/UVOT
57989.82	−0.44	18.84(0.07)	–	–	*Swift*/UVOT
57989.82	−0.44	–	–	20.04(0.10)	*Swift*/UVOT
...	...	...	...	...	...

Table A2. g-, r-, i-, z-filter observed (non-K-corrected, non-S-corrected) magnitudes (in AB system). Errors are in parentheses. The full table is available online as supplementary material.

MJD	r. f. phase from maximum	g	r	i	z	Instrument
57931.00	−54.55	21.10(0.20)	–	–	–	*Gaia*
57977.44	−11.83	17.30(0.20)	–	–	–	*Gaia*
57983.44	−6.31	17.07(0.02)	17.24(0.01)	17.33(0.02)	17.63(0.02)	GROND
57984.14	−5.67	–	17.23(0.06)	17.20(0.05)	–	LCO + Sinistro
...	...	...	...	...	...	...

Table A3. U-, B-, V-observed (non-K-corrected, non-S-corrected) magnitudes (in AB system). *Swift*/UVOT photometry was measured with a 5- arcsec radius aperture (see the text). Errors are in parentheses. The full table is available online as supplementary material.

MJD	r. f. phase from maximum	U	B	V	Instrument
57984.12	−5.68	–	17.36(0.05)	17.30(0.05)	LCO + Sinistro
57986.79	−3.23	–	17.23(0.01)	17.45(0.01)	LCO + Sinistro
57987.78	−2.31	–	17.33(0.01)	17.42(0.00)	LCO + Sinistro
57989.82	−0.44	17.48(0.05)	–	–	*Swift*/UVOT
...	...	...	...	...	...

Table A4. NIR-observed (non-K-corrected) template-subtracted (J, H) magnitudes and PSF (K_s) magnitudes (in AB system). Errors are in parentheses. The full table is available online as supplementary material.

MJD	r. f. phase from maximum	J	H	K_s	instrument
57983.44	− 6.31	17.75(0.02)	18.19(0.03)	18.68(0.08)	GROND
57996.40	5.61	17.72(0.05)	$\gtrsim 14.957$	18.64(0.12)	SOFI
58008.38	16.63	17.82(0.02)	18.13(0.04)	18.39(0.05)	GROND
58017.37	24.90	17.99(0.04)	18.40(0.05)	18.73(0.09)	GROND
...	...	...	...	...	...

Table A5. S-corrections for GROND bands.

MJD	g	r	i
57892.39	− 0.001	− 0.013	− 0.007
57984.39	0.053	− 0.002	− 0.030
57986.38	0.045	− 0.007	− 0.043
57987.38	0.047	− 0.009	− 0.040
58025.31	− 0.017	0.028	0.020
58045.28	− 0.057	0.008	0.022
58069.21	− 0.081	0.003	0.032
58102.20	− 0.066	− 0.010	0.037
58132.45	− 0.095	− 0.031	0.054
58135.22	− 0.075	− 0.030	0.036
58159.23	− 0.102	0.0560	− 0.074
58192.10	− 0.045	0.0570	− 0.052

Table A7. S-corrections for *Swift*/UVOT filters.

MJD	B	V
57892.39	− 0.000	0.013
57984.39	0.001	0.019
57986.38	− 0.001	0.010
57987.38	− 0.001	0.012
58025.31	0.006	0.049
58045.28	0.001	0.037
58069.21	− 0.001	0.019
58102.20	− 0.001	0.003
58132.45	− 0.012	− 0.017
58135.22	− 0.011	− 0.010
58159.23	− 0.024	− 0.004
58192.10	− 0.000	0.020

Table A6. S-corrections for Sinistro filters.

MJD	B	g	V	r	i	z
57892.39	0.000	0.001	0.004	− 0.016	− 0.009	− 0.005
57984.39	− 0.002	− 0.008	0.036	− 0.006	− 0.009	− 0.059
57986.38	− 0.002	− 0.006	0.024	− 0.005	− 0.013	− 0.057
57987.38	− 0.003	− 0.007	0.026	− 0.007	− 0.012	− 0.057
58025.31	− 0.003	0.013	0.010	− 0.007	0.000	− 0.054
58045.28	− 0.008	0.021	− 0.004	− 0.017	− 0.003	− 0.052
58069.21	− 0.006	0.018	− 0.013	− 0.014	− 0.003	− 0.049
58102.20	− 0.009	0.015	− 0.012	− 0.026	− 0.005	− 0.051
58132.45	− 0.006	− 0.001	− 0.014	− 0.027	− 0.007	− 0.009
58135.22	− 0.009	0.010	− 0.014	− 0.037	− 0.007	− 0.049
58159.23	− 0.013	0.024	− 0.014	0.056	− 0.007	− 0.008
58192.10	0.001	0.053	− 0.008	0.020	− 0.010	− 0.005

Table A8. Estimated uncertainties ΔS_{corr} for the filters U, z, J, H, K_s (for each instrument) divided in two temperature ranges (see the text). The full table is available online as supplementary material.

	$4000\,\mathrm{K} < T < 8000\,\mathrm{K}$	$8000\,\mathrm{K} < T < 12000\,\mathrm{K}$
GROND	$\Delta S_{\mathrm{corr},z} = 0.010\,\mathrm{mag}$	$\Delta S_{\mathrm{corr},z} = 0.002\,\mathrm{mag}$
	$\Delta S_{\mathrm{corr},J} = 0.004\,\mathrm{mag}$	$\Delta S_{\mathrm{corr},J} = 0.001\,\mathrm{mag}$
	$\Delta S_{\mathrm{corr},H} = 0.001\,\mathrm{mag}$	$\Delta S_{\mathrm{corr},H} = 0.000\,\mathrm{mag}$
	$\Delta S_{\mathrm{corr},K_s} = 0.010\,\mathrm{mag}$	$\Delta S_{\mathrm{corr},K_s} = 0.001\,\mathrm{mag}$
SOFI	$\Delta S_{\mathrm{corr},J} = 0.020\,\mathrm{mag}$	$\Delta S_{\mathrm{corr},J} = 0.002\,\mathrm{mag}$
	$\Delta S_{\mathrm{corr},H} = 0.080\,\mathrm{mag}$	$\Delta S_{\mathrm{corr},H} = 0.001\,\mathrm{mag}$
	$\Delta S_{\mathrm{corr},K_s} = 0.070\,\mathrm{mag}$	$\Delta S_{\mathrm{corr},K_s} = 0.120\,\mathrm{mag}$
...	...	...

Table A9. *K*-corrections expressed in magnitudes.

r. f. phase from maximum	UVW2	UVM2	UVW1	U	B	g	V	r	i	z	J	H	K_s
−7	0.39	0.51	0.26	0.04	−0.18	−0.18	−0.21	−0.23	−0.24	−1.55	−0.24	−0.25	−0.25
−5	0.37	0.5	0.26	0.04	−0.17	−0.17	−0.21	−0.24	−0.24	−0.24	−0.22	−0.22	−0.25
−4	0.35	0.49	0.26	0.04	−0.16	−0.15	−0.17	−0.16	−0.27	−1.45	−0.22	−0.23	−0.24
32	0.06	0.28	0.27	0.02	0.08	0.02	−0.07	−0.21	−0.14	−1.54	−0.16	−0.20	−0.22
51	−0.07	0.17	0.27	0.02	0.22	0.13	−0.02	−0.13	−0.16	−1.52	−0.15	−0.18	−0.21
73	−0.24	0.02	0.28	0.01	0.30	0.19	0.01	−0.08	−0.06	−1.60	0.58	−0.10	−0.20
103	−0.4	−0.13	0.28	0.01	0.26	0.15	−0.01	−0.05	−0.09	−1.45	0.18	−0.16	−0.19
135		0.244	0.179	0.006	0.023	−0.094	−1.455						
+ 175		0.164	0.097	−0.067	0.097	−0.131	0.096	1.64097	−0.16296	−0.19509			
+ 358		0.106	0.066	−0.085	0.066	−0.17	−0.378	−0.11968	−0.1644	−0.19602			

Table A10. Slopes of the observed LCs (10^{-2} mag d^{-1}).

UVW2	UVM2	UVW1	U	B	g	V	r	i	z	J	H	K_s
-	–	–	–	–	2.22	–	2.23	2.28	2.25	2.23	1.80	–

Table A11. Spectra in Fig. 5.

MJD	r. f. phase from maximum	Instrument	Resolution
57982.39	−7	EFOSC2	18.2
57984.39	−5	EFOSC2	17.9
57986.38	−4	EFOSC2	18.9
57987.38	−3	EFOSC2	27.2
58011.73	20	LCO + FLOYDS	21.1
58015.73	23	LCO + FLOYDS	21.8
58021.73	29	LCO + FLOYDS	22.1
58025.31	32	EFOSC2	17.9
58030.71	37	LCO + FLOYDS	20.0
58035.73	42	LCO + FLOYDS	18.4
58045.28	51	EFOSC2	17.8
58069.21	73	EFOSC2	17.8
58102.20	103	EFOSC2	17.8
58132.45	131	LRIS	–
58135.22	133	EFOSC2	18.0
58159.23	155	Binospec	–
58192.10	187	X-Shooter	–
58389.35	367	X-Shooter	–

Table A12. Logarithm of the bolometric luminosities integrated over the *UVW*2, *UVM*2, *UVW*1, *U*, *B*, *g*, *V*, *r*, *i*, *z*, *J*, *H*, K_s photometry, and the blackbody temperatures (expressed in Kelvin). Errors are reported in parenthesis. We fixed a maximum error for the blackbody temperatures to 2000 K (see the text). Epochs later than ∼160 d require even larger error bars. The full table is available online as supplementary material.

r. f. phase from maximum	$\log_{10} L_{bol}$	T_{BB}
−5.57	43.65(0.06)	11693.01
−4.94	43.63(0.06)	11487.76
−2.48	43.67(0.07)	11633.86
1.51	43.75(0.07)	11429.11
...	...	..

Table A13. Comparison of the metallicity estimated for SN 2017gci with the metallicities of a sample of nearby SLSNe I and GRBs (data from Chen et al. 2017b).

Object	SN 2017gci	SN 2017egm	PTF11hrq	PTF12dam	GRB 100316D	GRB 060505	GRB 111005A
Reference	Section 4.1	(Chen et al. 2017b)	(Cikota et al. 2017)	(Thöne et al. 2015)	(Izzo et al. 2018)	(Thöne et al. 2014)	(Tanga et al. 2017)
Redshift	0.087	0.031	0.057	0.107	0.059	0.089	0.013
PP04 O3N2	8.135 ± 0.07	8.77 ± 0.01	8.19 ± 0.01	8.01 ± 0.14	8.21 ± 0.02	8.24 ± 0.00	8.63 ± 0.03

Table A14. Best-fitting estimates of the physical parameters of SN 2017gci (with reference to Fig. 3). The TIGERFIT best-fitting model is listed in the first column with the assumed phase from the explosions in square brackets.

	Ejecta mass M_{ejecta} ($M_\odot$)	Mass accretion rate ($M_\odot$ year^{-1})	Polar magnitude field B_p (10^{14} G)	Initial period $P_{initial}$ (ms)	Phase from the explosion ϕ_0 (d)	Opacity κ (cm^2 g^{-1})	CSM mass ($M_\odot$)	Progenitor radius (10^{14} cm)	Diffusion time-scale (d)	Spin-down time-scale (d)
MF1	9.0	–	5.5	2.8	15.7	0.08	–	–	34.5	1.1
csm0 (30)	12.4	0.1	–	–	–	0.07	4.9	0.004	–	–

[1]*INAF – Osservatorio Astronomico di Padova, Vicolo dell'Osservatorio 5, I-35122 Padova, Italy*

[2]*Dipartimento di Fisica e Astronomia 'G. Galilei', Università di Padova, Vicolo dell'Osservatorio 3, I-35122 Padova, Italy*

[3]*Department of Astronomy, Oskar Klein Centre, Stockholm University, Albanova, SE-10691 Stockholm, Sweden*

[4]*Max-Planck-Institut für Extraterrestrische Physik, Giessenbachstraße 1, D-85748 Garching, Germany*

[5]*INFN, Sezione di Padova, Via Francesco Marzolo 8, I-35131 Padova, Italy*

[6]*School of Physics & Astronomy, Cardiff University, Cardiff, CF24 3AA, UK*

[7]*DTU Space, National Space Institute, Technical University of Denmark, Elektrovej 327, DK-2800 Kongens Lyngby, Denmark*

[8]*Department of Particle Physics and Astrophysics, Weizmann Institute of Science, Rehovot 7610001, Israel*

[9]*Finnish Centre for Astronomy with ESO (FINCA), University of Turku, Vesilinnantie 5, FI-20014, Turku, Finland*

[10]*Aalto University Metsähovi Radio Observatory, Metsähovintie 114, FI-02540 Kylmälä, Finland*

[11]*Department of Physics, University of California, Santa Barbara, CA 93106-9530, USA*

[12]*Las Cumbres Observatory, 6740 Cortona Dr, Suite 102, Goleta, CA 93117-5575, USA*

[13]*Center for Interdisciplinary Exploration and Research in Astrophysics (CIERA) and Department of Physics and Astronomy, Northwestern University, Evanston, IL 60208, USA*

[14]*Departamento de Física Teórica y del Cosmos, Universidad de Granada, E-18071 Granada, Spain*

[15]*Astronomical Observatory, University of Warsaw, Al. Ujazdowskie 4, PL-00-478 Warszawa, Poland*

[16]*Department of Physics and Astronomy, University of Southampton, Southampton, Hampshire SO17 1BJ, UK*

[17]*Center for Astrophysics | Harvard & Smithsonian, 60 Garden Street, Cambridge, MA 02138-1516, USA*

[18]*Department of Physics and Astronomy, University of Turku, Vesilinnantie 5, FI-20014 Turku, Finland*

[19]*Astrophysics Research Centre, School of Mathematics and Physics, Queens University Belfast, Belfast BT7 1NN, UK*

[20]*Birmingham Institute for Gravitational Wave Astronomy and School of Physics and Astronomy, University of Birmingham, Birmingham B15 2TT, UK*

[21]*Institute for Astronomy, University of Edinburgh, Royal Observatory, Blackford Hill EH9 3HJ, UK*

[22]*Department of Physics and Astronomy, University of California, 1 Shields Avenue, Davis, CA 95616-5270, USA*

This paper has been typeset from a TeX/LaTeX file prepared by the author.